

System-Level Experimental Evaluation of Reconfigurable Intelligent Surfaces for NextG Communication Systems

Maria Tsampazi, *Student Member, IEEE*, and Tommaso Melodia, *Fellow, IEEE*

Abstract—Reconfigurable Intelligent Surfaces (RISs) are a promising technique for enhancing the performance of Next Generation (NextG) wireless communication systems in terms of both spectral and energy efficiency, as well as resource utilization. However, current RIS research has primarily focused on theoretical modeling and Physical (PHY) layer considerations only. Full protocol stack emulation and accurate modeling of the propagation characteristics of the wireless channel are necessary for studying the benefits introduced by RIS technology across various spectrum bands and use-cases. In this paper, we propose, for the first time: (i) accurate PHY layer RIS-enabled channel modeling through Geometry-Based Stochastic Models (GBSMs), leveraging the QUAsi Deterministic RadIo channel GenerAtor (QuaDRiGa) open-source statistical ray-tracer; (ii) optimized resource allocation with RISs by comprehensively studying energy efficiency and power control on different portions of the spectrum through a single-leader multiple-followers Stackelberg game theoretical approach; (iii) full-stack emulation and performance evaluation of RIS-assisted channels with SCOPE/srsRAN for Enhanced Mobile Broadband (eMBB) and Ultra Reliable and Low Latency Communications (URLLC) applications in the world's largest emulator of wireless systems with hardware-in-the-loop, namely Colosseum. Our findings indicate (i) the significant power savings in terms of energy efficiency achieved with RIS-assisted topologies, especially in the millimeter wave (mmWave) band; and (ii) the benefits introduced for Sub-6 GHz band User Equipments (UEs), where the deployment of a relatively small RIS (e.g., in the order of 100 RIS elements) can result in decreased levels of latency for URLLC services in resource-constrained environments.

Index Terms—NextG Channel Modeling, Wireless Network Channel Emulators, Power Control, Energy Efficiency, Geometry-Based Stochastic Models, QuaDRiGa, Sub-6 GHz, millimeter wave, Enhanced Mobile Broadband, Ultra Reliable and Low Latency Communications.

I. INTRODUCTION

Undoubtedly, research in 5th generation (5G) wireless communication systems has been following an upward trend in recent years. 5G promises better connectivity anywhere, anytime, for everyone and everything, with increased coverage, better system capacity, extremely low latency [1], improved performance in terms of both energy and spectral efficiency [2], [3], while also simultaneously satisfying the diverse Quality of Service (QoS) demands of its heterogeneous users [4] across a variety of deployment scenarios and network topologies [5].

Copyright (c) 2025 IEEE. Personal use of this material is permitted. However, permission to use this material for any other purposes must be obtained from the IEEE by sending a request to pubs-permissions@ieee.org.

This article is based upon work partially supported by the U.S. National Science Foundation under grants CNS-1925601 and CNS-2112471.

M. Tsampazi, and T. Melodia are with the Institute for the Wireless Internet of Things, Northeastern University, Boston, MA, U.S.A. E-mail: {tsampazi.m, t.melodia}@northeastern.edu.

Hence, 5G and beyond technologies are expected to become an indispensable component of future smart environments [6]–[12]. Another prominent technology anticipated to accommodate the needs of future NextG communication networks are RISs. RISs have recently attracted widespread interest in the research community as a part of a smart city environment for 5G, and beyond 5G wireless communication systems [2], [13]–[26]. Indeed, RISs technologies have been proven to extend coverage [17]–[19], [23], enhance both spectral and energy efficiency [2], [27]–[29], while at the same time enabling the vision of smart and reconfigurable propagation environments [22], [26], [30], which can be controlled through Software-defined Radio (SDR) techniques [31], [32]. Therefore, due to both the tremendous advantages that they introduce (e.g., decreased levels of latency [33], [34]) and due to their presence in a multitude of use-cases scenarios (e.g., resource allocation in multi-UE Non-Orthogonal Multiple Access (NOMA) systems [35], localization and positioning [36], assisting anti-jamming methods [37], and enhancing Unmanned Aerial Vehicle (UAV)-enabled communications [34], [38]–[43] among others), there is a clear need for further understanding of RIS-assisted channels through effective performance evaluation campaigns in different spectrum bands and use cases.

In this article, we aim to provide, for the first time, a holistic, system-level evaluation of RIS-assisted channels for NextG communication systems in Cellular Vehicle-to-Everything (C-V2X) environments across different portions of the spectrum, while also paving the way for their evaluation across various network slices on experimental platforms. Our key contributions are as follows:

- 1) We leverage the capabilities of the fully reconfigurable, MATLAB-based [44] statistical ray-tracer QuaDRiGa [45], which uses Radio Frequency (RF) data collected under various conditions to cascade the wireless links and include the effect of a RIS in the topology.
- 2) We focus on a C-V2X setup comprising of a UAV serving as a flying Next Generation Node Base (gNB) for multiple UEs.
- 3) Through a single-leader multiple-followers Stackelberg game we jointly optimize the overall received signal strength at the gNB, and each UE's individual energy efficiency in a NOMA system.
- 4) Through this hierarchical game-theoretic approach, we determine both the phase shifts of the RIS reflecting elements, as well as the Uplink (UL) transmission power of the UEs for both the Sub-6 GHz and the mmWave bands.
- 5) We install the generated wireless topologies for the band

that requires only a minimal number of RIS elements to achieve a significant path gain enhancement in the Colosseum Wireless Network and Channel Emulator [46].

6) We modify the Radio Access Network (RAN) functionalities in terms of scheduling profiles (i.e., Round Robin (RR) and Waterfilling (WF)) and slicing (i.e., allocation of the available Physical Resource Blocks (PRBs)) and we observe the performance gain provided through the RIS technology on the eMBB and URLLC network slices.

A. Related Work

The current literature hosts a plethora of RIS simulators for PHY layer channel modeling across various operating frequencies. Additionally, substantial efforts have been reported in the design, creation, and real-world deployment of such surfaces. In [47], [48], the authors present the mmWave SimRIS simulator for indoor and microcell environments. The aforementioned works state that accurate PHY layer simulators that can operate in a variety of frequencies and applications, ideally using real data, are of utmost importance. The authors note that further research is needed to develop practical channel models for various propagation environments and to identify compelling use cases. Finally, the authors emphasize the need to explore the coexistence of eMBB and URLLC UEs in various frequency domains, as well as the importance of standardization and integration into existing networks. In [49] a commercial RIS simulator is leveraged to perform system-level simulation in the mid and mmWave bands within a real-world urban environment. The authors conclude by mentioning the importance of analytical frameworks for system-level analysis by using tools leveraging stochastic geometry. Regarding the sub-6 GHz band, in [50], a 3D GBSM relying on the statistical properties of the wireless channels is discussed, taking into account both multipath propagation and continuous-time evolution. A GBSM channel model incorporating a RIS is also considered in [51], highlighting the importance of leveraging small panels. Other NextG RIS-assisted channel models, which discuss path-loss propagation and take into account geometry, are also presented in [34], [52]. Rayleigh and Rician channels are used to model the multipath effect, and their integration in RIS-assisted communication systems is discussed in detail in [53], [54]. In [55], a frequency-independent channel model for RIS is discussed, whereas a RIS-assisted channel model for Vehicle-to-everything (V2X) environments that incorporates the Rician channel matrix is presented in [56]. A RIS-assisted channel modeling approach for high frequencies is discussed in [57], while a signal processing perspective on multipath propagation with RIS is given in [58]. Physics-based PHY models are presented in [59], [60], while other approaches include deploying RIS panels in the Sub-6 GHz [61] and mmWave [62] bands [63], [64], with a focus on energy efficiency [65].

Additionally, the contribution of RIS technology to energy efficiency through power control is a well-investigated topic. In [66], a non-convex optimization framework for energy efficiency that jointly optimizes the Transmitter (TX) power of the Base Station (BS) and the reflecting coefficients of the RIS on the Downlink (DL) is considered. In [67], the paper tackles

energy efficiency maximization in an UL RIS-aided mmWave NOMA network by jointly optimizing the UE TX power and the RIS phase shifts using iterative optimization techniques. In [68], the usage of both RISs and UAV is discussed in terms of providing energy-efficient communications on the DL while ensuring the QoS demands of the UEs. The proposed method uses Successive Convex Approximation (SCA) to iteratively determine a joint optimal solution for the UAV trajectory, RIS phase shifts, and the UAV TX power. In [69], the problem of energy efficiency maximization is modeled as a Mixed Integer Non-Linear Programming (MINLP) problem, with the objective of enhancing overall energy efficiency on the DL by optimizing the BS's TX power and RIS phase shifts. The work in [70] discusses the topic of energy efficiency maximization in a RIS-assisted network, where convex optimization and sequential approximation methods are employed to jointly optimize the TX powers of the UEs and the reflection coefficients of the RIS in the UL. In [71], a Machine Learning (ML) approach based on the Proximal Policy Optimization (PPO) algorithm for the maximization of energy efficiency in RIS-aided networks is discussed. The optimization problem is formulated under constraints of the rate requirement of the UEs, the power budget at the BS, and the discrete phase shift coefficients of each reflecting element at the RIS on the DL. In this approach, the BS's TX power and the phase shift matrix of the RIS are jointly optimized. Similarly, In [72], the joint energy efficiency maximization problem for a DL NOMA network is discussed, with the goal of jointly optimizing the beamforming vectors at the BS and the coefficient matrices at the RIS, while also controlling the TX power at the BS using Deep Reinforcement Learning (DRL). In [39], a two-tier Stackelberg game is used to jointly maximize the received signal strength at the evolved Node Base (eNB) by calculating the RIS phase shifts and the UEs' UL transmission power in RIS-assisted, UAV-enabled networks. However, the aforementioned framework does not consider the frequency of operation, and therefore provides limited insights on energy-efficient resource allocation on different portions of the spectrum. In [73], a Stackelberg game is also discussed for end-to-end (E2E) energy-efficient optimization through power control and RIS reconfiguration in UL RIS-assisted, UAV-enabled Integrated Access and Backhaul (IAB) networks. However, the focus is directed towards the low Sub-6 GHz portion of the spectrum, disregarding emerging 5G frequency bands, such as the mmWave.

Lastly, the generation of RF scenarios for Wireless Network Channel Emulators has been a trending topic. In [74], a framework for creating RF scenarios for large-scale, real-time wireless emulators such as Colosseum, leveraging a commercial ray-tracer is introduced. It leverages efficient clustering techniques and channel impulse response re-sampling to scale down the large input set of RF data to fewer parameters. In [75], the CaST Toolchain is presented. It comprises a framework for creating RF scenarios from ray-tracing models for Field Programmable Gate Array (FPGA)-based emulation platforms and a Software-defined Networking (SDN) channel sounder to characterize the emulated channels. In [76], a framework for creating mobile RF scenarios, including the presence of UAVs, based on real collected data, is discussed.

The contributions discussed above clearly demonstrate the significance of RIS-assisted NextG channel models, as well as the substantial gains achieved in terms of energy efficiency through the deployment of RISs in various heterogeneous scenarios and use cases. At the same time, the interest in the validation and testing of channel models, leveraging the full cellular protocol stack, in high-fidelity and accurate network channel emulators is ever-growing.

However, despite the established contributions of hierarchical game-theoretic approaches to energy efficient power control in wireless networks [77], [78], there has been limited research on the benefits of energy-efficient power control in RIS-assisted and UAV-enabled C-V2X networks in the Frequency Range 1 (FR1) and Frequency Range 2 (FR2). Moreover, despite the availability of frameworks for generating RF scenarios in channel emulators, no prior work has focused on installing RIS-assisted scenarios in these emulators. Consequently, a research gap exists in cross-layer experimental evaluation of RIS-assisted channels utilizing the full protocol stack on experimental platforms. Therefore, the evaluation of RIS-assisted networks across different network slices (e.g., eMBB and URLLC) is currently missing. This paper aims to fill these gaps in the literature with the following original contributions: (i) we propose accurate PHY layer RIS-enabled channel modeling through GBSMs and QuaDRiGa; (ii) we cascade the generated channels to include the effect of a RIS; (iii) we leverage hierarchical game theory to optimize the RIS elements' phase shifts; (iv) we study energy-efficient power control across different spectrum bands; (v) we implement the RIS-assisted channels on the Colosseum testbed; and (vi) we perform full-protocol stack emulation using srsRAN [79] to evaluate the performance gain in eMBB and URLLC network slicing by fine-tuning the BS's network functions.

The remainder of this paper is organized as follows. Section II provides an overview on GBSM-based NextG channel modeling with QuaDRiGa. Section III discusses the simulation of a RIS-assisted C-V2X setup with QuaDRiGa, as well as its evaluation on energy efficiency in the Sub-6 GHz and the mmWave bands. Section IV details the installation and evaluation of a RIS-assisted topology on the Colosseum wireless network and channel emulator, as well as its evaluation on the eMBB and URLLC network slices. Finally, Section V concludes the paper and discusses possible future directions.

II. GBSMs WITH QUADRIGA

A. Channel Modeling with QuaDRiGa

The implementation of GBSMs is fairly simple and computationally inexpensive, and can be done through code-based simulators (e.g., NYUSIM [81], WINNER II/+ [82] and 3GPP-3D [83]), and Standardized Channel Models (e.g., the Spatial Channel Model (SCM), IMT-Advanced, METIS, mmMAGIC and the 5G-ALLSTAR [84]). QuaDRiGa extends the WINNER and 3GPP-3D models [85], with the advantage that it achieves a high level of precision [86]. It takes as input configuration files to describe a propagation scenario, and each file contains a parameter table with statistical information about the wireless channels (i.e., delay spread, Rician K-factor, shadow fading,

Cross-polarization Ratio (XPR), angular spread values and their properties such as correlation and distribution). The aforementioned files were created through the process of channel sounding either with measurements performed in urban cities [87], [88], or by the incorporation of statistical tables such those included in [89]. The modeling procedure can be divided into two parts: (i) a stochastic part that generates the Large Scale Parameters (LSPs), e.g., path loss, shadowing and fading, and (ii) a geometry-based part that calculates the updated Small Scale Parameters (SSPs), e.g., delay spreads [90]. In contrast to the classical ray-tracing approach, QuaDRiGa does not use an exact geometric representation of the propagation environment. The distribution of the scattering clusters (e.g., tree foliage and buildings) is random. This adds simplicity into the implementation and decreases the computational cost without accuracy loss. QuaDRiGa simulates complicated NextG heterogeneous environments [91], by considering effects such as dual-mobility, 3D propagation and continuous time evolution. The generated parameters are spatially correlated, while the wide-sense stationary (WSS) properties are kept both within a segment and during mobility. Finally, the simulation steps can be summarized as follows [86], [87], [92].

- 1) **Definition of the UE Input Variables.** The topology layout is defined (i.e., TXs/Receivers (RXs)), location (i.e., coordinates) and antenna characteristics (i.e., carrier frequency and type). Second, the nodes' trajectories and their speed profile are determined. Last, a propagation scenario is set (Line-of-Sight (LOS)/Non-Line-of-Sight (NLOS), or a combination). Examples of supported scenarios [86], [87], [93] are:
 - a) **Berlin/Dresden UMa**
 - Terrestrial *macrocell* parameters extracted from measurements in Germany.
 - b) **WINNER model**
 - *UMa C1 & C2*: For *macrocell* BSs in urban & suburban areas, respectively.
 - *UMi B1*: For *microcell* BSs in urban areas.
 - c) **3GPP TR 37.885 Highway V2X**
 - *NLOS* due to dynamic blockages (e.g., vehicles).
 - d) **3GPP TR 38.901 NR model - UMa & UMi**
 - For center frequencies between 0.5 and 100 GHz.
- 2) **Calculation of LSPs.** Out of the aforementioned parameter tables, the LSPs are calculated. At this step, sources of scattering have been created, according to the multi-bounce approach, comprising a First Bounce Scatterer (FBS) and a Last Bounce Scatterer (LBS).
- 3) **Generation of the XPR.** Antenna characteristics and polarization effects are taken into account.
- 4) **Calculation of the Channel Coefficients and Path Gain Generation.** The results of the previous steps alongside with SSPs (e.g., angular characteristics of the paths) are combined to calculate the channel coefficients (i.e., the Multipath Components (MPCs)). A last fine-tuning of the shadow fading and path loss parameters, alongside with the Rician factor are applied to produce the final path gains.

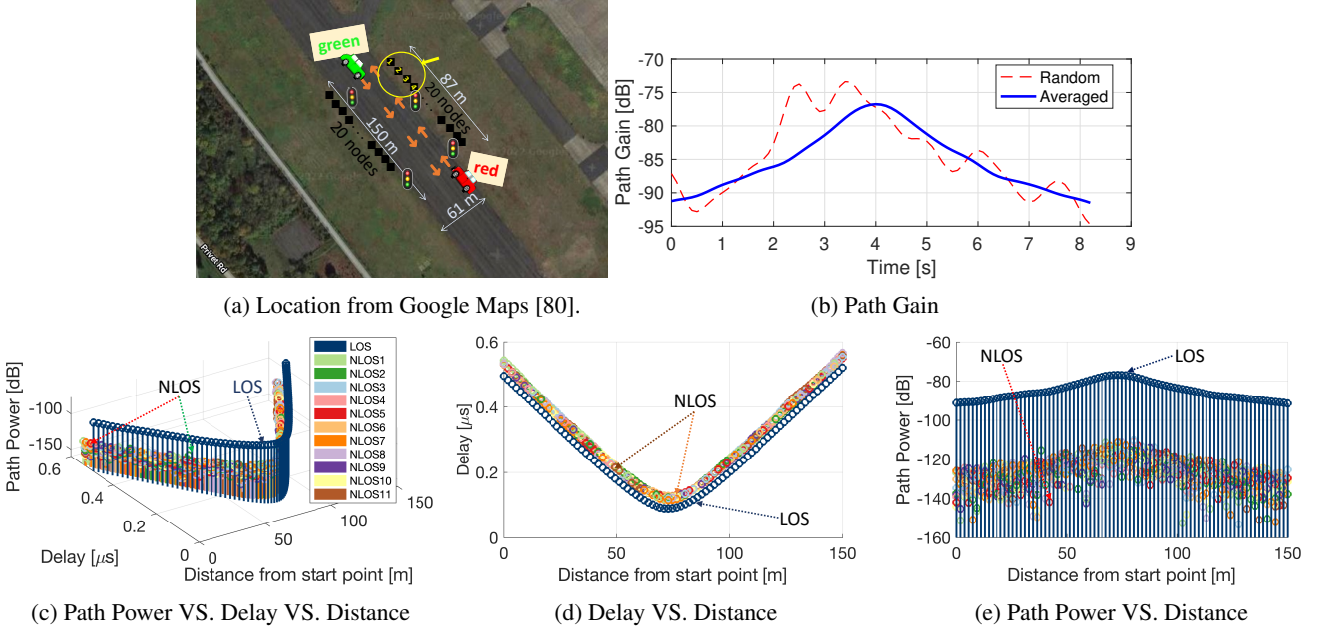


Fig. 1: Results averaged over 100 channel realizations for the link describing green vehicle’s transmission to the red in Willow Grove Naval Air Base in Horsham Township, Pennsylvania, USA.

5) **Repetition of steps 1–4 for successive channel traces and final Propagation Channels.** In case of mobility the process is repeated. All individual components produced by every step of the aforementioned procedure are combined to obtain the final channels.

B. Experimentation through Simulation with QuaDRiGa

To test the software’s effectiveness, we generate a C-V2X setup [94] in which two vehicles approach each other under the 3GPP 37.885 Highway LOS transmission conditions (Section II-A). Both have a steady speed of 66 km/h for a distance of 150 m. The vehicles are equipped with omni-directional antennas mounted on their roof at 1.5 m and operate at the center frequency of 5.9 GHz. As it can be seen from the topology in Fig. 1a, scattering objects such as 4 Road Side Units (RSUs) alongside with 40 nodes on the highway’s sides, placed 5 m apart, representing other parked cars, are also present. The simulation’s location corresponds to the Willow Grove Naval Air Base in Horsham Township, Pennsylvania, USA (Global Positioning System (GPS) coordinates for latitude and longitude are [40.202951, −75.149008]), and the conversion from GPS to Cartesian coordinates has been done with MATLAB’s [44] `latlon2local` function. Given the stochastic nature of the channels, and in order to obtain a good estimate, we observe the results every 0.1 s and average them over 100 channel realizations. In Fig. 1, we present the simulation’s results, when the green transmits to the red vehicle, as depicted in Fig. 1a. In Fig. 1b the continuous bell-shaped curve represents the averaged path gains, while the dotted represents the path gains for a random setup. The log-distance path loss [94] model leveraged in the channel generation, explains the increase in path gains as the path loss decreases, particularly for a minimal distance between the vehicles. In the final path gain values in Fig. 1b, the main contribution comes from the direct LOS component,

while the contribution of the NLOS MPCs is weighted to be insignificant, based on the input configuration file. In Fig. 1c, we include a 3D plot of the generated path powers versus delay and travelled distance, while in Fig. 1d and in Fig. 1e, we observe Fig. 1c from two different perspectives. 12 paths are generated, one for the direct path, and 11 for the multiple copies of the signal, for each position of the mobile TX/RX (i.e., Fig. 1e). In Fig. 1d, the path power of the LOS path attains a lower delay value compared to its NLOS counterparts for a given distance. As the vehicles begin to approach each other, the delay values decrease, reaching their minimum around the midpoint of the track, where the two vehicles cross.

C. GBSMs for Wireless Network Channel Emulators

We install the aforementioned scenario in Colosseum, a publicly available testbed comprising 128 Standard Radio Nodes (SRNs). It consists of pairs of Dell PowerEdge R730 servers and NI USRP X310 SDRs that enable large-scale experimentation in diverse network deployments via the Massive Channel Emulator (MCHEM) component. MCHEM leverages FPGA-based Finite Impulse Response (FIR) filters to replicate wireless environment conditions such as path loss, fading, attenuation, mobility, and interference pre-modeled through ray-tracing software, analytical models, or real-world measurements. The Colosseum Traffic Generator (TGEN), built on top of the Multi-Generator (MGEN) Transmission Control Protocol (TCP)/User Datagram Protocol (UDP) traffic generator [95], emulates different traffic profiles (e.g., multimedia content), demand, and distributions (e.g., Poisson, periodic), by emulating Internet Protocol (IP) traffic flows between the SRNs.

We focus on nodes 1 → 4 as depicted in Fig. 1a, which share a bandwidth of 10 MHz. Nodes 1 → 2 are deployed through the srsRAN protocol stack [79], while nodes 3 → 4 are deployed with the Wi-Fi Stack, which is based on the open-source GNU

Radio implementation of the IEEE 802.11a/g/p standard [96]. Cellular node 1 and Wi-Fi node 3 are BSs, while nodes 2 and 4 serve as the respective cellular and Wi-Fi UEs. Finally, UDP traffic is generated with *iPerf*. In Figs. 2a and 2b, we illustrate the UL cellular Signal to Interference plus Noise Ratio (SINR) and throughput between the cellular nodes. Initially, an average SINR of 27 dB is observed, which drops to 22 dB, when the WiFi nodes start transmitting at 20 dB (at approximately $t = 120$ s), before slightly recovering to ~ 24 dB. Similarly, the UL throughput becomes unstable once WiFi transmissions commence.

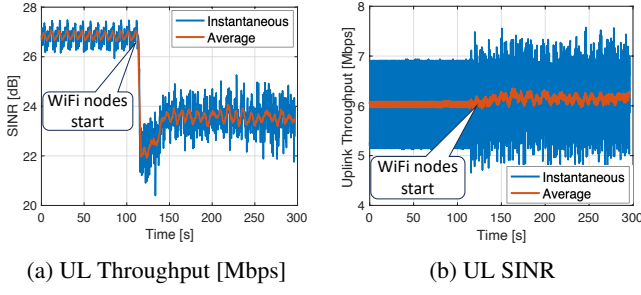


Fig. 2: UL cellular metrics between BS-node 1 and UE-node 2.

Conclusively, with this simple yet richly detailed use-case, we are able to verify the suitability of QuaDRiGa and GBSMs for generating RF scenarios for Colosseum, as well as the efficiency of the latter in generating and managing traffic among heterogeneous nodes. Notably, although the aforementioned scenario comprises multiple nodes, the focus is directed towards the aforementioned to demonstrate the software's capabilities, and hence an extensive evaluation is omitted. Readers interested in the creation of RF scenarios for Colosseum can refer to [46], [74], [75].

III. INVESTIGATING ENERGY EFFICIENCY WITH FREQUENCY-DEPENDENT GBSMS AND RISs IN C-V2X

Evidently, QuaDRiGa is effective in providing accurate geometric-based stochastic channel modeling. Additionally, considering that the generated channels are frequency-dependent, QuaDRiGa poses as an ideal candidate for investigating energy efficient power allocation across different spectrum bands and various use-cases. In this Section, we focus particularly on a C-V2X use-case [97] involving a UAV acting as a flying gNB serving multiple UEs, to investigate energy efficiency in the Sub-6 GHz and mmWave bands. Without loss of generality, we assume that the BS simulated with QuaDRiGa is a static UAV hovering at a certain height, while the generated channels are cascaded to simulate the inclusion of a RIS in the topology. We believe that the strong LOS links provided by the UAV and the cascaded channels offered by RIS technology fit into the description of a C-V2X scenario for NextG wireless environments and smart cities as described in [39].

A. System Model: A RIS-assisted C-V2X setup with QuaDRiGa

As illustrated in Fig. 3, a RIS-assisted and UAV-enabled wireless communications system is evaluated on the UL direction. Specifically, the topology comprises of a UAV, a building

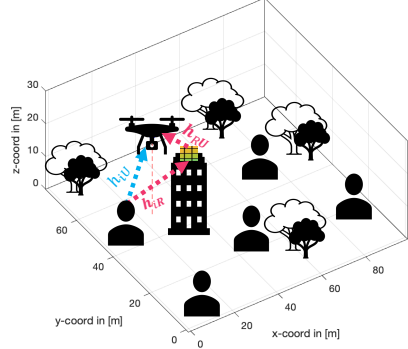


Fig. 3: RIS-assisted and UAV-enabled communications system.

facade hosting a RIS and a set of mobile UEs, denoted as $I = \{1, \dots, i, \dots, |I|\}$, which communicate directly with the UAV. The RIS consists of $|M|$ reflecting elements, the set of which is defined as $M = \{1, \dots, m, \dots, |M|\}$, and each RIS element's phase shift is $\theta_m \in [0, 2\pi], \forall m \in M$. Finally, the corresponding diagonal phase-shift matrix is defined as $\Theta = \text{diag}(e^{j\theta_1}, \dots, e^{j\theta_m}, \dots, e^{j\theta_{|M|}})$. The incoming signals at the UAV are combined, as in [39], so as each UE's i signal is the outcome of the coherent addition of the direct and the reflected signal. The channel gain of the direct link between a user i and the UAV is described as h_{iU} , the channel gain between a user i and the RIS is defined as h_{iR} , where h_{iR} can also be written as $\mathbf{h}_{iR} = [|h_{iR,1}|e^{j\omega_1}, \dots, |h_{iR,m}|e^{j\omega_m}, \dots, |h_{iR,|M|}|e^{j\omega_{|M|}}]^T$, and finally, the channel gain of the reflected link from the RIS to the UAV is denoted as \mathbf{h}_{RU} . Subsequently, the cascaded channel is given as $\mathbf{h}_{RU}^H \Theta \mathbf{h}_{iR}$. Last, the steering vector for the UE i to the RIS LOS link is defined as $\mathbf{h}_{iR}^{LOS} = [1, e^{-j\frac{2\pi}{\lambda}d\phi_{iR}}, \dots, e^{-j\frac{2\pi}{\lambda}(|M|-1)d\phi_{iR}}]^T$, while the steering vector for the RIS to the UAV LOS link is denoted as $\mathbf{h}_{RU}^{LOS} = [1, e^{-j\frac{2\pi}{\lambda}d\phi_{RU}}, \dots, e^{-j\frac{2\pi}{\lambda}(|M|-1)d\phi_{RU}}]^T$. Moving forward, we keep using the same notation as in [39], which is also reported in Table I. The first RIS element, i.e., $m = 1$, with its respective coordinates, i.e., (x_R, y_R, z_R) [m], is used as a reference point in the following calculations, while for the UAV, its coordinates are given as follows (x_U, y_U, z_U) [m]. It is noted that in [39], the featured channel model is frequency-independent. In our study, we aim at observing the impact of the frequency of operation in terms of energy efficiency on realistic RIS-assisted wireless channels on two different 5G bands, namely the Sub-6 GHz and the mmWave band. It is highlighted that RISs are expected to work across multiple frequency ranges, including both the FR1 and FR2 bands [98], to ensure interoperability across diverse deployment scenarios and applications. Given that QuaDRiGa can reliably support the simulation of channels up to 100 GHz, as mentioned in Section II, the Sub-6 GHz and mmWave bands are chosen. Therefore, we experiment with two different values for the center frequency, i.e., 5.9 GHz and 28 GHz, respectively. Finally, both the UEs and the UAV are equipped with single-antenna omni-directional TXs/RXs. It is noted that although omni-directional antennas are commonly used in the Sub-6 GHz band [99]–[104], and they can be deployed on mmWave communication systems [105]–[109], this is not typical [110]. Instead, high-directional antennas are

most commonly used in such scenarios [111]–[113], to combat severe propagation loss and achieve high antenna gains. Within the scope of this work, we focus on the use of omni-directional antennas for the mmWave to provide insights into the performance enhancement introduced by RIS in cases where omni-directional antennas are convenient for deployment, such as in a C-V2X environment [114]. While it is indeed true that in a dynamic environment such as the aforementioned, a directional antenna can improve Received Signal Strength Indicator (RSSI), this increased directionality comes at the cost of precise alignment with the RIS and UEs. Therefore, continuous beam tracking and adaptation are needed, which introduce additional overhead and latency that may outweigh the benefits of directive gains. Additionally, highly accurate and precise channel modeling with directional antennas in urban C-V2X environments, where the effects of multipath propagation are strong, can prove rather challenging, mainly due to the narrow mmWave beams, which lead to position deviations, inaccuracies, and alignment errors, resulting in beam misalignment, signal loss, and significant performance drops.

TABLE I: Channel Modeling Notation

Symbol	Description
$ I $	Number of mobile UEs
I	Set of mobile UEs
$ M $	Number of reflecting elements on the RIS
M	Set of RIS's reflecting elements
$\theta_m, \forall m \in M$	Reflecting element's phase shift
\mathbf{h}_{RU}	Channel Gain for the RIS to UAV reflected link
Θ	Diagonal phase-shift matrix
\mathbf{h}_{iR}	Channel Gain for the UE i to RIS link
$\mathbf{h}_{RU}^H \Theta \mathbf{h}_{iR}$	Cascaded Channel Gain
h_{iU}	Channel Gain for the UE i to UAV direct link
$d_{RU}[m]$	Euclidean distance between the RIS and the UAV
$d_{iR}[m]$	Distance between the UE i and the RIS
$d_{iU}[m]$	Distance between the UE i and the UAV
ϕ_{RU}	Cosine of the signal's AoD for the RIS to the UAV link
ϕ_{iR}	Cosine of the signal's AoA for the UE i to RIS link
$\lambda[m]$	Carrier wavelength
$d[m]$	Antenna separation
\mathbf{h}_{RU}^{LOS}	Steering vector for the RIS to the UAV LOS link.
\mathbf{h}_{iR}^{LOS}	Steering vector for the UE i to the RIS LOS link.
h'_{xy}	MPC Gain, where $x \in \{i, R\}$, $y \in \{R, U\}$
$ h'_{xy} , \varphi'_{xy}$	Magnitude and phase of the MPC
$ N $	Number of generated MPCs

Last, the channels in [39], from which our use-case is inspired, rely on the Rice and Rayleigh mathematical models to emulate the wireless links. However, their simple yet effective implementation may not accurately represent real-world wireless environments [51]. For these reasons, we proceed by creating the channels with QuaDRiGa. The channel generation process is described in Section II-A, where for each generated link a number of MPCs is produced based on the Channel Generator's input scenario, in our case the 3GPP-compliant scenario, 3GPP_38.901_UMa. Finally, we assume that the links between the UEs and the UAV are NLOS, while those remaining, i.e., the channels between the UEs and the RIS, and the RIS to UAV, are LOS. The transmission conditions of the aforementioned links were selected to ensure that the cascaded channel created by the RIS is strong enough to redirect the UEs'

signals to the UAV, for both the Sub-6 GHz and, especially, the mmWave band, which suffers from transmission losses. The wireless channels are observed every 0.1 s and for their creation, the steps listed below are followed:

- Generate scenario-based MPCs (i.e., h'_{xy}) for every link.
- Perform coherent summation of the MPCs [74] to obtain the link's channel gain, as reported in (1)

$$h''_{xy} = \sum_{j=1}^{|N|} |h'_{xy}| \cdot e^{j\varphi'_{xy}}. \quad (1)$$

- Average the channel gains (i.e., h''_{xy}) over a 100 different channel realizations to obtain the link's *final* channel gain (e.g., h_{iU}).
- Multiply the generated channels with the corresponding steering vectors, i.e., \mathbf{h}_{RU}^{LOS} and \mathbf{h}_{iR}^{LOS} , to get the respective final channel gains (i.e., \mathbf{h}_{RU} , \mathbf{h}_{iR}).

The overall channel power gain for the UE i to UAV link is denoted as $G_i = |h_{iU} + \mathbf{h}_{RU}^H \Theta \mathbf{h}_{iR}|^2$, and the UEs are able to communicate concurrently with the UAV thanks to the NOMA technique. The received channel gains (i.e., G_i) at the UAV are sorted and decoding starts from the UE with the highest channel gain. Finally, the UAV's RX decodes the received superposed signal with the help of the Successive Interference Cancellation (SIC) technique, which is implemented on its end. The interference sensed by each UE is defined as follows in (2):

$$I_i = \sum_{j < i} G_j P_j + I_0, \quad (2)$$

where P_j [W] is the UL TX power of the UE j and I_0 is the power of the zero-mean Additive White Gaussian Noise (AGWN). Each UE's achieved SINR is given as follows in (3):

$$\gamma_i = \frac{P_i G_i}{I_i}. \quad (3)$$

B. Hierarchical Game-Theoretic Power Control

In this Section, we aim to study how the frequency-dependent GBSM-based system model presented in Section III-A will impact the energy efficiency in both the Sub-6 GHz and mmWave bands. In brief, both the UEs and the UAV indulge in a single-leader multiple-followers Stackelberg Game, where the target is to jointly maximize the UAV's overall received signal strength and each UE's energy efficiency in a distributed manner. In detail, the UAV acting as a leader computes the RIS elements' effective phase shifts (and intelligently steers the signals reflected by the RIS) with a goal to enhance its received signal quality. In turn, the UEs, acting as followers, observe the leader's action and through the formulation of a non-cooperative game aim at maximizing their energy efficiency, by determining their optimal UL TX power. Each UE's utility function is defined in (4):

$$U_i(P_i, \mathbf{P}_{-i}) = \frac{W \cdot (1 - e^{-\alpha \gamma_i})^M}{P_i}, \quad (4)$$

where \mathbf{P}_{-i} is the TX power vector of all the UEs except for UE i , W [Hz] is the system's bandwidth, and $\alpha, M \in \mathbb{R}^+$ are parameters which control the utility function's slope. The

adopted utility function for energy efficiency represents the trade-off between the achieved QoS satisfaction, i.e., SINR, and the invested UL TX power [39], [115]. In detail, the numerator of the utility function, i.e., $(1 - e^{-\alpha\gamma_i})^M$ is a sigmoidal curve which expresses the UE satisfaction, with respect to its QoS demands, while the denominator expresses the associated cost with reference to the transmission power levels. Because of the nature of the sigmoidal curve, small increases in γ_i (by increasing the TX power) will initially improve the utility. However, increasing γ_i further requires significant power while providing diminishing returns in utility. As a result, the optimal strategy is to transmit at lower power levels in order to maintain higher energy efficiency.

Finally, the joint optimization problem is formulated as follows, with the respective problem solved by the UAV written as:

$$\max_{\boldsymbol{\theta}} \sum_{\forall i \in I} P_i |h_{iU} + \mathbf{h}_{RU}^H \boldsymbol{\Theta} \mathbf{h}_{iR}|^2 \quad (5a)$$

$$\text{s.t. } 0 \leq \theta_m \leq 2\pi, \forall m \in M. \quad (5b)$$

With regards to the optimization problem solved by the UEs, the latter ones participate in a non-cooperative game defined as $G = [I, \{A_i\}_{\forall i \in I}, \{U_i\}_{\forall i \in I}]$. In detail, I is the set of UEs (e.g., players), $A_i = [P_i^{\min}, P_i^{\max}]$ is each UE's strategy set, and U_i is their utility function. P_i^{\min} [W] and P_i^{\max} [W] correspond to each UE's minimum and maximum UL TX power levels respectively, where P_i^{\min} , is determined by the SIC prerequisite at the UAV's RX as follows:

$$G_i P_i - I_i \geq P_{tol}, \forall i \in \{2, \dots, i, \dots, |I|\}, \quad (6)$$

such that each UE's signal is decoded successfully. According to (6), each UE's signal strength, i.e., $G_i P_i$, should be greater than or equal to the UE's i sensed interference I_i , which is broadcasted by the UAV to all the UEs, plus a minimum acceptable power level $P_{tol} \in \mathbb{R}^+$, which represents the SIC RX's tolerance/sensitivity. Finally, the maximum UL TX power level P_i^{\max} is imposed by the maximum power budget of the UE's device. The optimization problem is finally determined as follows:

$$\max_{P_i \in A_i} U_i(P_i, \mathbf{P}_{-i}) = \frac{W \cdot (1 - e^{-\alpha\gamma_i})^M}{P_i}, \forall i \in I \quad (7a)$$

$$\text{s.t. } G_i P_i - I_i \geq P_{tol}, \forall i \in \{2, \dots, i, \dots, |I|\} \quad (7b)$$

$$P_i \leq P_i^{\max}, \forall i \in I. \quad (7c)$$

The non-cooperative game's, G , outcome is a Nash equilibrium, which determines the UEs' optimal TX power vector, i.e., $\mathbf{P}^* = [P_1^*, \dots, P_i^*, \dots, P_{|I|}^*]$.

The solution of the optimization problem taking place on the UAV's side and defined in (5a)-(5b) is the RIS elements' effective phase shifts' vector $\boldsymbol{\theta}^*$. It is noted that to maximize the overall received signal strength, the UAV only needs to calculate the effective RIS elements' phase shifts (i.e., $\boldsymbol{\theta}^*$) that maximize the overall channel power gain of the UEs. The aforementioned optimization problem is non-convex, making it challenging to find a globally optimal solution. As described in [39], [40], when there is a single UE in the system, the optimal

phase shifts of the RIS elements are given by the following closed-form solution:

$$\theta_m^* = \angle h_{iU} + \omega_m + \frac{2\pi}{\lambda} d(m-1) \phi_{RU}, \forall m \in M. \quad (8)$$

To derive the closed-form phase-shift solution in (8) and maximize the received signal strength at the UAV, we aim to achieve phase alignment of the received signals from different transmission paths. Notably, this can be achieved through coherent signal construction of the incoming signals at the UAV. Indeed, the UE's channel power gain is maximized when the direct signal and the signal reflected by the RIS are perfectly aligned and coherently combined at the UAV's RX [40]. This generally holds true when the phase shifts of the direct and the cascaded signals are equal, as follows $\angle h_{iU} = \angle (\mathbf{h}_{RU}^H \boldsymbol{\Theta} \mathbf{h}_{iR})$. Therefore, there's an optimal $1 \times |M|$ phase-shift vector $\boldsymbol{\theta}^* = \angle \mathbf{v}$ for the single-UE case. Similarly, in the multi-UE case, there exists a distinct reflection-coefficient vector $\mathbf{v}_i = [v_{i,1}, \dots, v_{i,|M|}] \in \mathbb{C}^{|M| \times 1}$ for each UE i that maximizes its channel power gain. In the multi-UE case, the solution to the leader's maximization problem is a linear combination of the phase shifts of the RIS elements that enhances each UE's signal strength, with the reflection-coefficient vectors \mathbf{v}_i being distinct for each UE.

On the other hand, the optimization problem solved on the UEs' side will result in the determination of their optimal UL TX power vector \mathbf{P}^* , as mentioned, since given the RIS elements' effective phase shifts, each UE determines its optimal UL TX power P_i^* via non-cooperatively interacting with the rest of the UEs in the action space. The Stackelberg equilibrium of this hierarchical game-theoretic approach can be given as $(\boldsymbol{\theta}^*, \mathbf{P}^*)$.

Definition 1: (Nash Equilibrium) The UL TX power vector $\mathbf{P}^* = [P_1^*, \dots, P_i^*, \dots, P_{|I|}^*]$ is a Nash equilibrium of the non-cooperative game $G = [I, \{A_i\}_{\forall i \in I}, \{U_i\}_{\forall i \in I}]$ if for every UE $i \in I$, it holds that $U_i(P_i^*, \mathbf{P}_{-i}) \geq U_i(P_i, \mathbf{P}_{-i}), \forall P_i \in A_i$.

At the Nash equilibrium, the UE has no incentive to improve its achieved utility by altering its transmission power strategy, given the strategies of the rest of the players (i.e., the other UEs).

Theorem 1: (Existence & Uniqueness of a Nash Equilibrium) For the non-cooperative game given as $G = [I, \{A_i\}_{\forall i \in I}, \{U_i\}_{\forall i \in I}]$, there exists a unique Nash equilibrium point, which is defined as follows:

$$P_i^* = \max\{P_i^{\min}, \min\{\frac{\gamma_i^* \cdot I_i}{WG_i}, P_i^{\max}\}\}, \forall i \in I, \quad (9)$$

where γ_i^* represents the unique positive solution to the equation $\frac{\partial f(\gamma_i)}{\partial \gamma_i} \gamma_i - f(\gamma_i) = 0$, $f(\gamma_i) = (1 - e^{-\alpha\gamma_i})^M$.

The Theorem's proof relies on the quasi-concavity property of the utility function $U_i(P_i, \mathbf{P}_{-i})$ with respect to the UL TX power P_i . The quasi-concavity property is proven and further explained in [115], which also provides a reference guide with detailed steps of the proof. Therefore, given the RIS elements' effective phase shifts $\theta_m^*, \forall m \in M$, and the optimal transmission power vector $P_i^*, \forall i \in I$, the Stackelberg equilibrium is iteratively determined as presented in Fig. 4. Notably, the convergence of the UEs' strategies to the Nash equilibrium point is achieved through the implementation of a Best Response Dynamics algorithm [115], as further detailed

in Algorithm 1. Note that the superscript (j) indicates the iterations required for the non-cooperative game played among the UEs. Additionally, it is highlighted that the maximum TX power levels for the UEs (as defined in Step 3 of Algorithm 1) are determined by 3GPP standards and are set to 23 dBm [116]–[118]. The corresponding minimum value is set to -20 dBm.

Algorithm 1 Stackelberg Game-Theoretic Optimization

- 1: Initialize the network topology, including the locations of UEs, RIS, and the UAV.
- 2: Generate the channels using QuaDRiGa, as described in Section III-A.
- 3: Initialize randomly $P_i \in [10^{-5}, P_i^{\max}]$.
- 4: Determine RIS elements' phase-shift adaptation by solving (5a)–(5b) and calculate $G_i, \forall i \in I$.
- 5: Sort users according to G_i , so decoding starts from the UE with the highest channel gain.
- 6: Set $j = 0$.
- 7: **repeat**
- 8: Set $j = j + 1$.
- 9: **for** $i \in I$ **do**
- 10: Determine the optimal UL TX power $P_i^*(j)$ by solving (7a)–(7c).
- 11: **end for**
- 12: **until** $|P_i^*(j) - P_i^*(j - 1)| \leq \epsilon, \forall i \in I$, where $\epsilon \approx 10^{-4}$.

We consider the following setup, where a UAV hovers at the point $(x_U = 25, y_U = 50, z_U = 25)$ [m] of the three-dimensional space serving a NOMA cluster of $|I| = 5$ users. Their distance from the RIS is given as $d_{i,R} = [20, 27, 37, 58, 66]$ [m] and all are randomly distributed around the RIS's reference point, which is given as $(x_R = 30, y_R = 40, z_R = 20)$ [m]. The system's bandwidth is equal to $W = 10$ MHz, and the AGWN power is $I_0 = -140$ dBm for the Sub-6 GHz and $I_0 = -160$ dBm for the mmWave band, respectively. It is noted that AGWN noise is already added in the final path gain values through QuaDRiGa [86]. Specifically, in QuaDRiGa, AGWN noise is used to generate spatially correlated LSPs, which statistically characterize the propagation environment. These LSPs indirectly shape the multipath environment and influence path gain. Thus, the AGWN values (i.e., I_0), which are included in the calculation of the UE's interference, represent reference noise levels. Indeed, these two distinct values are a correction applied to the the UEs' sensed interference, i.e., I_i , defined in (2), so as the optimization framework can be evaluated for the respective spectrum bands under the same configuration of the utility's slope control parameters, defined as $a = 0.3$ and $M = 3$. Finally, the frequencies are centered to 5.9 and 28 GHz for the respective bands, the mobile UEs' maximum power budget is set to $P_i^{\max} = 23$ dBm, and the sensitivity of the UAV's RX is set to be equal to $P_{tol} = -150$ dBm.

It is finally noted that in the following, the performance evaluation of the RIS-assisted and UAV-enabled communication system depicted in Fig. 3 will take place under 10, 100, and 1000 RIS elements for *both* the Sub-6 GHz and the mmWave band. Although it generally holds true that for a given RIS dimension, a mmWave RIS will host a higher number of RIS

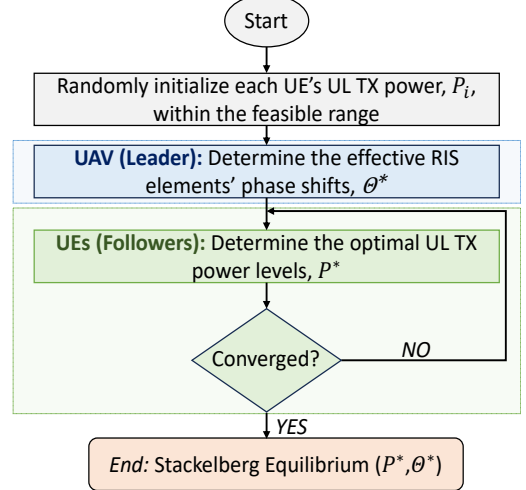


Fig. 4: A Hierarchical Stackelberg Game-Theoretic Approach to Energy-Efficient Power Control.

elements than a Sub-6 GHz RIS, given the same element spacing (e.g., $\lambda/2$), increasing the number of elements onboarded on the RIS also increases the complexity of its handling [65]. Consequently, a trade-off emerges between hosting thousands of RIS elements and maintaining ease of operation, particularly when experimenting in the mmWave band, where location inaccuracies are of utmost importance. For the aforementioned reasons, investigating the number of the elements onboarded on the RIS is deemed necessary.

The outcomes of the hierarchical game-theoretic power allocation in the Sub-6 GHz and mmWave bands are observed by considering the allocated UL TX power level and achieved UE utility both independently and collectively. In Fig. 5, we observe each UE's allocated UL TX power (Figs. 5a, 5c) and achieved utility (Figs. 5b, 5d), versus their respective index under different number of RIS's reflecting elements both for the Sub-6 GHz and the mmWave band. All UEs are sorted in descending order with reference to their channel gains, where the lowest index represents the UE with the highest channel gain, and the highest UE index corresponds to the one with the lowest channel gain. Notably, the framework's power control [39] enables low channel gain UEs to transmit with lower power levels and achieve higher utilities. This behavior can be explained by the utility function which is affected by the UE's channel-gain-to-interference ratio, i.e., $\frac{G_i}{I_i}$, at the exponent of the utility's numerator (see (4)). In detail, low channel gain UEs usually exhibit a low channel-gain-to-interference ratio which forces the maximum point of the utility function to take a low power value (i.e., P_i). This pattern is clearly illustrated in Fig. 5 where we also observe that as the number of RIS's reflecting elements increases, their achieved utilities also increase (Figs. 5b, 5d), whereas the UEs' allocated UL TX powers decrease (Figs. 5a, 5c), as expected. With regards to the two bands under study, in Fig. 5a we observe that for the Sub-6 GHz band, 100 reflecting elements on the RIS are enough for efficient power control, while for the mmWave band, a minimum of 1000 elements is needed as seen in Fig. 5c. This is due to the high propagation losses of the latter band [119], which stress the need for bigger RIS surfaces [62] to enable effective

beamforming and therefore more efficient power allocation.

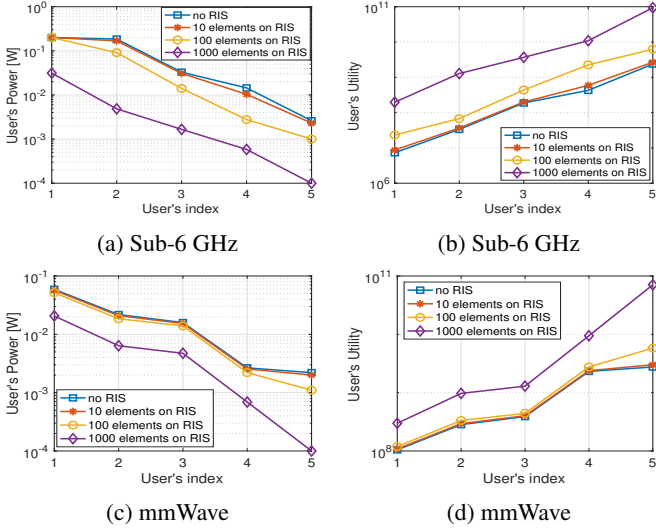


Fig. 5: Evaluation of the hierarchical game-theoretic power control framework per UE, under different number of RIS elements and different bands.

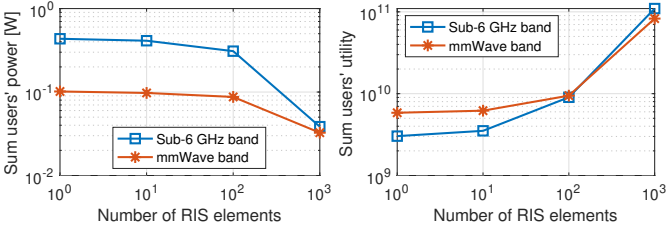


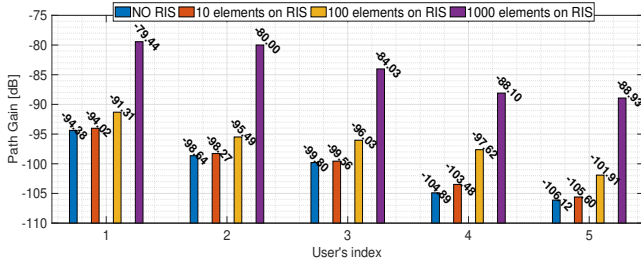
Fig. 6: Evaluation of the hierarchical game-theoretic power control framework on the entire system, under different number of RIS elements and different bands.

The overall performance gain of the entire system (e.g., the NOMA cluster) is illustrated in Fig. 6, where we observe both the sum UEs' allocated power levels and utilities as a function of a different number of RIS elements both for the Sub-6 GHz and the mmWave band. We can deduce that for a small number RIS elements (e.g., 10^1 RIS elements), the system's performance is comparable to the case without a RIS (i.e., 100 RIS elements). When the number of RIS elements increases, the sum UEs' powers decreases while their sum utility/satisfaction increases, as expected. Notably, the increased number of RIS elements results in the reduced sum of UEs' powers and thus in their increased sum utility/satisfaction. We also observe that even if the system follows the same power allocation trend in the two bands, the sum of the allocated powers to the mmWave UEs is lower compared to the case of their Sub-6 GHz counterparts. It is reminded that the devised utility function for energy efficiency, captures the trade-off between increasing γ_i (which improves the QoS) and minimizing P_i (which reduces power consumption). Since the increase in γ_i is limited by a low $\frac{G_i}{I_i}$, increasing P_i will lead to diminishing returns in the numerator of the utility function. In detail, when the ratio $\frac{G_i}{I_i}$ is low, the SINR i.e., $\gamma_i = \frac{P_i G_i}{I_i}$ becomes small. In this case, the exponential term $e^{-\alpha \gamma_i}$ approaches 1, meaning that even if

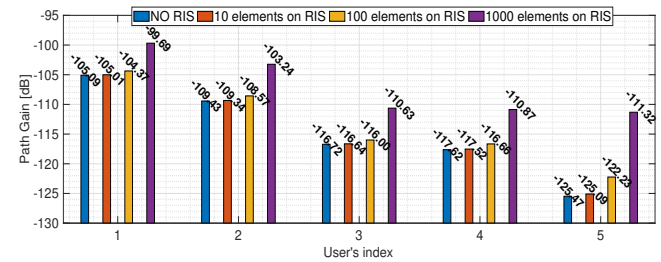
the UE increases P_i , the utility does not increase significantly because the SINR is limited by the high interference. Thus, the utility function reaches its maximum at a lower power level P_i because increasing power doesn't significantly improve the SINR. Therefore, UEs with low $\frac{G_i}{I_i}$ transmit at lower power levels to avoid unnecessary energy consumption, as increasing P_i will not substantially improve their utility. Our power control framework favors UEs with lower $\frac{G_i}{I_i}$ to transmit with lower power levels. In our work, mmWave UEs experience low $\frac{G_i}{I_i}$ levels, and hence have a lower Channel Quality Information (CQI) compared to the UEs of the Sub-6 GHz band they are compared to. As a result when ultimately compared, given the low $\frac{G_i}{I_i}$ levels of the former, they get to transmit with lower power levels compared to their Sub-6 GHz counterparts.

Finally, in Fig. 7, we present the path gains, PG_i , for every UE, i , with and without the inclusion of the RIS both for the Sub-6 GHz and the mmWave band. All the UEs are sorted in descending order, and thus the UE with the lowest index is the UE with the best channel gain conditions, while the UE with the biggest index corresponds to the UE with the worst channel. Specifically, Fig. 7a depicts the path gains for the Sub-6 GHz band with the carrier frequency centered at 5.9 GHz. Based on the reported findings, the performance achieved with a minimum of 10 RIS elements closely resembles the performance without the RIS. A noticeable difference at $\sim |1.41|$ dB between the aforementioned cases is only observed for index 4, which, within the scope of this work, indicates a UE with *poor* CQI. Discernible differences can be observed for all the UEs when focusing on the cases of 100 or 1000 RIS elements. In detail, an average difference of $\sim |4|$ dB is observed when collectively comparing all the UEs without and with the existence of RIS in the topology under 100 RIS elements. Specifically, among all the UEs, the UE with index 4, achieves the most notable difference, by achieving a $|7.27|$ dB higher value at -97.62 dB in the presence of 100 RIS elements. In the absence of RIS, the corresponding value is reported at -104.89 dB. Last, the benefits of including 1000 elements on RIS are clearly illustrated in Fig. 7a, where the average path gain value for all the UEs considered is marked at -84.1 dB, $\sim 16.5\%$ higher compared to the average value of -100.77 dB achieved without the RIS inclusion.

Fig. 7b depicts the path gains obtained for the mmWave band with the carrier frequency centered at 28 GHz. Contrary to the findings of the conducted evaluation in the Sub-6 GHz, in the mmWave band, a minimum number of 1000 RIS elements is required to achieve distinguishable differences between the cases with and without a RIS. In this band, the UE that significantly benefits from the RIS technology with 1000 onboarded elements is the UE that experiences the worst CQI conditions, identified by UE ID 5. Specifically, the latter UE reports a $|14.15|$ dB higher value at -111.32 dB compared to the case without the RIS, where the path gain is marked at -125.47 dB. On average, UEs under the presence of 1000 RIS elements in the topology report path gains $\sim |7.72|$ dB or $\sim 7\%$ higher than in the absence of RIS. Precisely, the average path gain value of the UEs in the case of 1000 RIS elements is reported at -107.15 dB, while in the case of RIS absence this value is



(a) Sub-6 GHz band



(b) mmWave band

Fig. 7: Path Gains for two different Spectrum bands.

indicated at -114.87 dB.

Conclusively, in the Sub-6 GHz band, the average path gain value reported with 100 RIS elements is marked at -96.5 dB, a value $\sim 4\%$ higher than the average path gain of -100.77 dB reported in the absence of RIS. In the mmWave band, with 1000 RIS elements, the corresponding increase is found to be $\sim 7\%$. Based on these findings, a minimum number of 100 RIS elements is deemed necessary to support the deployment of RIS in the Sub-6 GHz band, while in the mmWave this number is found to be 1000.

It is finally noted that the performance evaluation of the Stackelberg game-theoretic optimization process involved elements in increasing orders of magnitude, representing successive powers of 10. The aforementioned numbers not only represent typical values encountered in the literature [58], [65], but also meet the requirements outlined in [98], which state that existing RIS elements can range from 10 elements and above. In the following, we also provide a performance evaluation under different sets of RIS elements for the respective bands, aiming to determine the minimal number of RIS elements each band requires to achieve higher levels of energy efficiency. Based on the experimental results in Fig. 8, it is noted that for the Sub-6 GHz band, 500 RIS elements result in similar performance to 1000 (Figs. 8a and 8b), while discernible performance improvements are observed from 100 elements and above, with 300 being an indicative value. For the mmWave band, it is noted that the respective values are 700 (resulting in similar performance to 1000) and 500 (indicative value for performance improvement), correspondingly (Figs. 8c and 8d).

C. Comparison with the state-of-the-art

In this section, we evaluate our optimization framework using two different utilities for energy efficiency, as shown in Table II. The utility function proposed in our work is labeled *Proposed Utility* and is compared with the utility presented in [73], referred to as *Literature Utility*. To assess the performance of our proposed method in comparison with [73], we also consider a NOMA cluster of 4 UEs, a bandwidth of 5 MHz, and the same noise levels as in [73], and we evaluate the performance in the Sub-6 GHz band. Finally, we consider two cases: one without the inclusion of a RIS and the other with 100 RIS elements onboard.

The performance evaluation results reported in Fig. 9 clearly indicate the suitability of the proposed utility function in yielding lower transmission power levels (Fig. 9a) and achieving

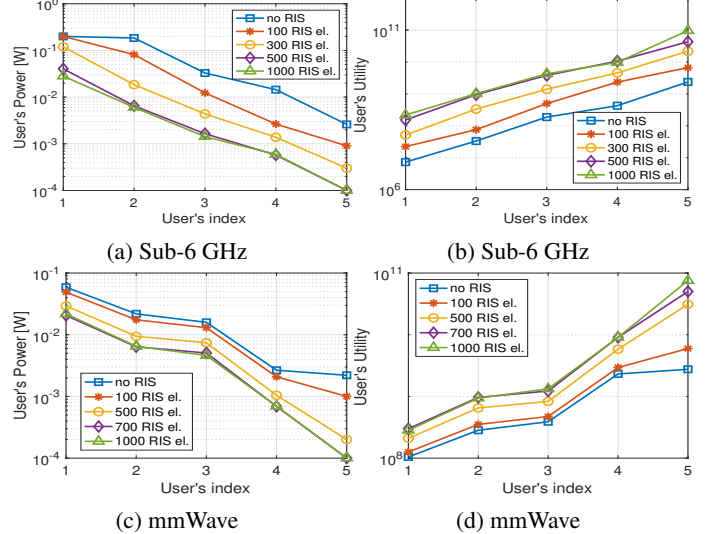


Fig. 8: Evaluation of the hierarchical game-theoretic power control framework per UE, under different number of RIS elements per each band.

TABLE II: Utility Functions Comparison

Proposed Utility:	$U_i(P_i, \mathbf{P}_{-i}) = \frac{W \cdot (1 - e^{-\alpha \gamma_i})^M}{P_i}$
Literature Utility:	$EE_i(P_i, \mathbf{P}_{-i}) = \frac{W \cdot \log_2(1 + \gamma_i)}{P_i}$

higher energy efficiency (Fig. 9b). This is due to the flexible design of our proposed utility through the control parameters, as well as its effective capture of the trade-off between achieving higher QoS and lower costs (e.g., reduced TX power levels).

IV. PERFORMANCE EVALUATION OF RIS-ASSISTED C-V2X COMMUNICATION SYSTEMS ON COLOSSEUM

As mentioned in Section III-B, the optimization problem solved by the UAV and defined in Eqs. 5a-5b, will result in the maximization of its total received signal strength through the individual maximization of each UE's incoming signal strength. Indeed, the latter is achieved through a linear combination of the RIS elements' effective phase shifts as given in (8), which will enable the creation of the cascaded channels denoted as $\mathbf{h}_{RU}^H \Theta \mathbf{h}_{iR}$. In consistency with Section III-A, all the incoming UE signals at the UAV are the result of the coherent summation of the direct, i.e., h_{iU} , and reflected signals. It is reminded that the path gains of the corresponding generated channels, without

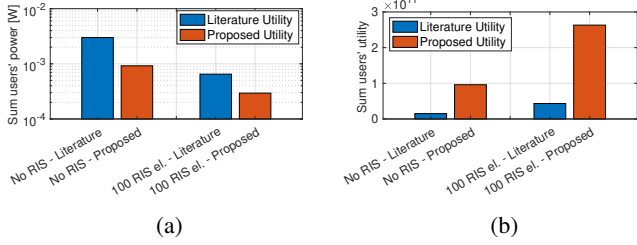


Fig. 9: Evaluation of the hierarchical game-theoretic power control framework under two different utilities given in Table II.

and with the inclusion of a different number of RIS elements are provided and illustrated in Fig. 7.

As a next step, we proceed by installing the generated channels in Colosseum. In summary, the reference input scenario to be installed includes two key components: the path gain, represented as a complex coefficient value in the form of FIR, and the Time-of-Arrival (ToA) value. The path gain is derived from the coherent summation of generated MPCs across the wireless links and has been averaged across multiple experiments, as detailed in Section III-A. Meanwhile, the ToA values have been computed based on the Euclidean distance between the entities considered in the topology (i.e., UAV, RIS, and UEs), given the speed of light (i.e., 3×10^8 [m/s]). These values collectively contribute to generating the time-variant Channel Impulse Response (CIR) for each node pair within the topology. Finally, a tutorial on the installation of RF scenarios in Colosseum can be found in [46], [75], but as it is not the focus of this paper, the detailed explanation is omitted.

We focus on the case of the Sub-6 GHz band, where all the wireless channels were simulated with QuaDRiGa at the center frequency of 5.9 GHz. We only consider the scenario with 100 RIS elements for all the RIS-assisted generated channels. This approach allows us to explore how a relatively small number of RIS elements (typically large arrays are required [120], [121]), and an average numerical increase of $\sim 4\%$ in the path gains between cases with and without RIS in the topology, can significantly improve network performance. Additionally, since previous results (see Section III) have shown that mmWave UEs are mostly benefited in terms of energy efficiency (i.e., they get to transmit with lower power levels, especially for 1000 RIS elements, while simultaneously satisfying their QoS demands), we aim at examining the advantages introduced by RIS technology in a realistic NextG RAN scenario tested in the Sub-6 GHz band. It is noted that although the channels were created at the frequency of 5.9 GHz using the QuaDRiGa channel modeling simulator, the testing frequency for this scenario in Colosseum is set to 1 GHz, which is the frequency that the MCHEM is optimized to work [122].

We leverage the capabilities of the SCOPE framework [123] to deploy an end-to-end RAN and core network though the srsRAN [124] softwarized open-source protocol stack on Colosseum. Specifically, we deploy a 3GPP-compliant cellular network comprising a single BS (i.e., the UAV) and 5 UEs distributed across 2 different slices. These are: (i) eMBB that concerns high traffic modeling of high-quality multimedia content and streaming applications, and (ii) URLLC for time-sensitive applications, such as autonomous driving in V2X

scenarios as detailed in [125]. Slice-based traffic is generated by the MGEN TCP/UDP traffic generator [95], based on the following specifications: eMBB UEs request 4 Mbps constant bitrate, while URLLC UEs generate 89.3 kbps Poisson traffic. The bandwidth of the BS is set equal to 10 MHz (i.e., 50 PRBs), and it is divided between the 2 slices. Specifically, we allocate 45 PRBs on the eMBB, while the remaining ~ 5 PRBs are assigned on the URLLC. In this way, we allocate 90% of the available resources to eMBB, which has the greatest demand for higher throughput. Consequently, 10% of the available resources are allocated to support the requirements for low latency on the URLLC. Among the 5 users considered, 3 of them are URLLC UEs, while the remaining 2 are assigned on the eMBB slice. It is also noted that the UEs of the eMBB are those who reported the highest path gain values, while the UEs of the URLLC are the ones with the lowest reported CQI values. With this allocation, we aim at exploring how the presence of the RIS in the topology will benefit the URLLC slice in a scenario where limited resources are available to serve 60% of the available UEs, especially when they experience poor transmission conditions (e.g., in the absence of RIS in the topology). Finally, the Key Performance Measurement (KPM) observed for eMBB is the DL throughput, while the respective value for URLLC is the buffer occupancy as a proxy for latency [125].

By using SCOPE's open Application Programming Interfaces (APIs), we fine-tune the RAN's functionalities, in terms of scheduling profile selection. Specifically, two Medium Access Control (MAC)-layer scheduling algorithms are compared, namely the RR and a fairer one, the WF, in all possible combinations. In Table IV, we present all the configurations considered in terms of scheduling profiles (defined in Table III) for the eMBB and URLLC slices, which define how PRBs are internally allocated to UEs belonging to each slice [126].

TABLE III: Scheduling Profiles Catalog

RR:	Round Robin
WF:	Waterfilling

TABLE IV: Scheduling Profiles Configuration

Setup ID	eMBB	URLLC
1	RR	RR
2	RR	WF
3	WF	RR
4	WF	WF

The results of this comparative performance evaluation can be seen in Fig. 10. Finally, all subsequent results were produced by taking the median as the most representative statistical value of a dataset, and averaged over multiple repetitions of experiments in the DL direction of the communication system¹.

In Figs. 10a and 10b, we focus on the case where both slices are served under the same scheduling policy. Based on the reported findings, when focusing on the eMBB slice, all

¹Note that all channels generated with QuaDRiGa in the RIS-assisted and UAV-enabled scenarios are reciprocal. The focus of this Section is the evaluation of a RIS-assisted and UAV-enabled communication system on the DL direction.

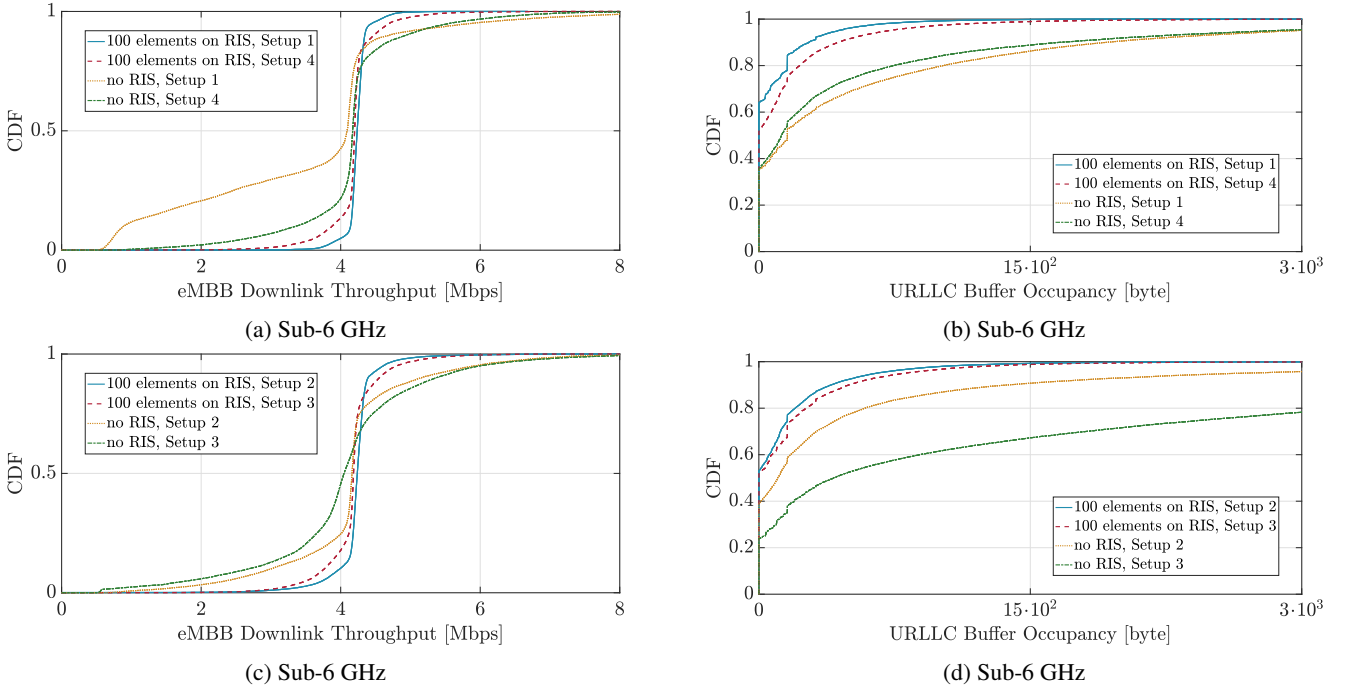


Fig. 10: Evaluation of a slice-based Multi-UE C-V2X communication system on Colosseum with and without the inclusion of RIS under different scheduling profiles.

configurations, both with and without the RIS inclusion, deliver a median throughput value of ~ 4 Mbps. However, Setup 1 achieves one of the highest reported throughput values of 4.236 Mbps with 100 RIS elements. The corresponding value in the absence of RIS is found to be 4.091 Mbps. With Setup 4 and 100 onboarded RIS elements, the median throughput value reaches 4.2 Mbps. The respective value in the absence of RIS is reported at 4.172 Mbps. On the URLLC slice, however, in the absence of RIS, both Setups 1 and 4 underperform compared to the case where RIS is included in the topology. Specifically, with Setup 1, the median value of the buffer size is reported at 158 byte, while for Setup 4, the corresponding value is marked at 127 byte. In both setups with RIS, a median value of 0 byte buffer occupancy is achieved, indicating zero latency.

In Figs. 10c and 10d we include the results collected when both slices are served under different scheduling policies. On the eMBB, Setup 2 achieves the highest throughput value reported in the presence of 100 elements on RIS at 4.238 Mbps, while Setup 3 achieves one of the lowest at 4.184 Mbps. The respective values in the absence of RIS are reported at 4.163 Mbps and 4.048 Mbps, correspondingly. On the URLLC, in the presence of RIS, all setups resulted in empty buffers, reporting a median value of 0 buffer occupancy. In the absence of RIS, with Setup 2 the median value for buffer occupancy is marked at 105 byte, while with Setup 3 the corresponding value is found to be 412 byte.

In Tables V and VI, all the results obtained without and with the inclusion of 100 RIS elements under different combinations of scheduling policies are collectively presented. Based on the reported findings in Table V we observe that in the presence of RIS in the topology, Setups 1 and 2 deliver almost identical performance on the eMBB, reporting median throughput values of 4.236 Mbps and 4.238 Mbps, respectively. Setups 3 and 4 de-

liver slightly worse performance, at 4.184 Mbps and 4.2 Mbps, correspondingly. On the URLLC, all setups resulted in optimal performance by achieving a median value of 0 byte buffer occupancy. The findings of Table VI indicate that in the absence of RIS in the topology, Setups 2 and 4 yield similar performance, achieving median eMBB throughput values of 4.163 Mbps and 4.172 Mbps. The aforementioned setups also lead to improved URLLC performance among those compared, achieving buffer occupancies of 105 and 127 byte, respectively. Setups 1 and 3 achieve eMBB throughputs of 4.091 Mbps and 4.048 Mbps eMBB, respectively. The median values for buffer occupancy on the URLLC are 158 and 412 byte, with the latter being the highest recorded in the absence of RIS in the topology. It is noted that all setups resulted in empty buffers on the URLLC when RIS was included in the topology. In the absence of RIS, the reported median values for buffer occupancy vary around the average value of 200 byte and are included in Table VI. When RIS is not included in the topology, all configurations result in increased buffer sizes, indicating higher levels of latency.

Conclusively, in resource-constrained environments (e.g., limited availability of PRBs), where the UEs may experience relatively poorer CQI conditions, the presence of RIS enhances the QoS experience of the URLLC by resulting in a buffer occupancy of 0 byte.

TABLE V: KPMs for RIS-assisted and UAV-enabled C-V2X topologies.

Setup ID	eMBB [Mbps]	URLLC [byte]
1	4.236	0
2	4.238	0
3	4.184	0
4	4.2	0

TABLE VI: KPMs for UAV-enabled C-V2X topologies without RIS.

Setup ID	eMBB [Mbps]	URLLC [byte]
1	4.091	158
2	4.163	105
3	4.048	412
4	4.172	127

V. CONCLUSION

In this work, we have leveraged QuaDRiGa's open-source code to simulate a RIS-assisted and UAV-enabled C-V2X topology which we evaluated under a different number of RIS elements both in the Sub-6 GHz and the mmWave portion of the spectrum. Through the formulation of a hierarchical - one leader - multiple followers - Stackelberg-based game-theoretic optimization framework, we were able to study the achieved energy efficiency of the topology on the aforementioned bands. Our results on power control indicate significant power savings and UE satisfaction, specifically for the mmWave band. Finally, while focusing on the case of 100 elements mounted on the RIS and the Sub-6 GHz band, we installed the generated channels on the Colosseum wireless network emulator and conducted an evaluation campaign under different setups of scheduling profiles, considering a fixed PRB allocation for both the eMBB and URLLC network slices. The performance evaluation results from network emulation on Colosseum indicate that in resource-limited conditions (i.e., a low number of allocated PRBs), the presence of RIS will counteract potential network degradation by resulting in empty buffers, thus ensuring low latency levels on the URLLC slice. Some interesting extensions of the current work include focusing on the study of stochastic UE mobility on the Colosseum Network Emulator and exploring the expected improvements introduced by the coexistence of RISs and UAVs, particularly in eliminating potential network coverage holes. Additionally, comparing QuaDRiGa RIS-assisted channels with other RIS-aided schemes and traditional beamforming represents an interesting direction for future research.

REFERENCES

- [1] H. Attar, H. Issa, J. Ababneh, M. Abbasi, A. A. Solyman, M. Khosravi, R. Said Agieb *et al.*, “5G System Overview for Ongoing Smart Applications: Structure, Requirements, and Specifications,” *Computational Intelligence and Neuroscience*, vol. 2022, 2022.
- [2] M. J. Shehab, I. Kassem, A. A. Kutty, M. Kucukvar, N. Onat, and T. Khattab, “5G networks towards smart and sustainable cities: A review of recent developments, applications and future perspectives,” *IEEE Access*, vol. 10, pp. 2987–3006, 2021.
- [3] S. Sobhi-Givi, M. G. Shayesteh, and H. Kalbkhani, “Energy-efficient power allocation and user selection for mmWave-NOMA transmission in M2M communications underlaying cellular heterogeneous networks,” *IEEE Transactions on Vehicular Technology*, vol. 69, no. 9, pp. 9866–9881, 2020.
- [4] H. Zhang, N. Liu, X. Chu, K. Long, A.-H. Aghvami, and V. C. Leung, “Network slicing based 5G and future mobile networks: Mobility, resource management, and challenges,” *IEEE communications magazine*, vol. 55, no. 8, pp. 138–145, 2017.
- [5] C.-X. Wang, J. Bian, J. Sun, W. Zhang, and M. Zhang, “A survey of 5G channel measurements and models,” *IEEE Communications Surveys & Tutorials*, vol. 20, no. 4, pp. 3142–3168, 2018.
- [6] I. Lopes, T. Guarda, A. Fernandes, and M. I. Ribeiro, “How 5G Will Transform Smart Cities: A Literature Review,” in *International Conference on Computational Science and Its Applications*. Springer, 2023, pp. 70–81.
- [7] L. Liu, X. Guo, and C. Lee, “Promoting smart cities into the 5G era with multi-field Internet of Things (IoT) applications powered with advanced mechanical energy harvesters,” *Nano Energy*, vol. 88, p. 106304, 2021.
- [8] A. Sharif, J. Guo, J. Ouyang, S. Sun, K. Arshad, M. A. Imran, and Q. H. Abbasi, “Compact base station antenna based on image theory for UWB/5G RTLS embraced smart parking of driverless cars,” *IEEE Access*, vol. 7, pp. 180 898–180 909, 2019.
- [9] D. Marabissi, L. Mucchi, R. Fantacci, M. R. Spada, F. Massimiani, A. Fratini, G. Cau, J. Yunpeng, and L. Fedele, “A real case of implementation of the future 5G city,” *Future Internet*, vol. 11, no. 1, p. 4, 2018.
- [10] Y. Jiang, W. Xiao, R. Wang, and A. Barnawi, “Smart urban living: Enabling emotion-guided interaction with next generation sensing fabric,” *IEEE Access*, vol. 8, pp. 28 395–28 402, 2019.
- [11] X. Zhao, H. Askari, and J. Chen, “Nanogenerators for smart cities in the era of 5G and Internet of Things,” *Joule*, vol. 5, no. 6, pp. 1391–1431, 2021.
- [12] J. E. Sánchez-Cano, W. X. García-Quilachamin, J. Pérez-Véliz, J. Herrera-Tapia, and K. A. Fuentes, “Review of methods to reduce energy consumption in a smart city based on IoT and 5G technology,” *iJOE*, vol. 17, no. 08, p. 5, 2021.
- [13] B. Rana, S.-S. Cho, and I.-P. Hong, “Review paper on hardware of reconfigurable intelligent surfaces,” *IEEE Access*, 2023.
- [14] P. Zivuku, S. Kisseleff, V.-D. Nguyen, K. Ntontin, W. A. Martins, S. Chatzinotas, and B. Ottersten, “Maximizing the Number of Served Users in a Smart City using Reconfigurable Intelligent Surfaces,” in *IEEE Wireless Communications and Networking Conference (WCNC)*, 2022, pp. 494–499.
- [15] A. Al Amin, J. Hong, V.-H. Bui, and W. Su, “Emerging 6G/B6G wireless communication for the power infrastructure in smart cities: Innovations, challenges, and future perspectives,” *Algorithms*, vol. 16, no. 10, p. 474, 2023.
- [16] S. Kisseleff, W. A. Martins, H. Al-Hraishawi, S. Chatzinotas, and B. Ottersten, “Reconfigurable intelligent surfaces for smart cities: Research challenges and opportunities,” *IEEE Open Journal of the Communications Society*, vol. 1, pp. 1781–1797, 2020.
- [17] R. Liu, M. Li, H. Luo, Q. Liu, and A. L. Swindlehurst, “Integrated sensing and communication with reconfigurable intelligent surfaces: Opportunities, applications, and future directions,” *IEEE Wireless Communications*, vol. 30, no. 1, pp. 50–57, 2023.
- [18] M. Salah, A. Pitsillides, and A. S. Mubarak, “Paving the way for economically accepted and technically pronounced smart radio environment,” *China Communications*, vol. 19, no. 8, pp. 247–266, 2022.
- [19] A. U. Makari, K. M. Rabie, O. Kaiwartya, K. Adhikari, X. Li, M. Quiroz-Castellanos, and R. Kharel, “Reconfigurable intelligent surfaces-enabled vehicular networks: A physical layer security perspective,” *arXiv preprint arXiv:2004.11288*, 2020.
- [20] M. Kamruzzaman, “Key technologies, applications and trends of internet of things for energy-efficient 6G wireless communication in smart cities,” *Energies*, vol. 15, no. 15, p. 5608, 2022.
- [21] L. Bariah, H. Sari, and M. Debbah, “Digital twin-empowered smart cities: A new frontier of wireless networks,” *Authorea Preprints*, 2023.
- [22] T. Dagiuklas, “The journey from 5G towards 6G,” in *8th International Symposium on Electrical and Electronics Engineering (ISEEE)*. IEEE, 2023, pp. 14–18.
- [23] J. Li, “From Liquid Crystal on Silicon and Liquid Crystal Reflectarray to Reconfigurable Intelligent Surfaces for Post-5G Networks,” *Applied Sciences*, vol. 13, no. 13, p. 7407, 2023.
- [24] P. Mishra and G. Singh, “6G-IoT Framework for Sustainable Smart City: Vision and Challenges,” in *Sustainable Smart Cities: Enabling Technologies, Energy Trends and Potential Applications*. Springer, 2023, pp. 97–117.
- [25] C. Masouros, J. A. Zhang, F. Liu, L. Zheng, H. Wymeersch, and M. Di Renzo, “Guest Editorial: Integrated Sensing and Communications for 6G,” *IEEE Wireless Communications*, vol. 30, no. 1, pp. 14–15, 2023.
- [26] M. D. Renzo, M. Debbah, D.-T. Phan-Huy, A. Zappone, M.-S. Alouini, C. Yuen, V. Sciancalepore, G. C. Alexandropoulos, J. Hoydis, H. Gacanin *et al.*, “Smart radio environments empowered by reconfigurable AI meta-surfaces: An idea whose time has come,” *EURASIP Journal on Wireless Communications and Networking*, vol. 2019, no. 1, pp. 1–20, 2019.
- [27] T. Hou, Y. Liu, Z. Song, X. Sun, Y. Chen, and L. Hanzo, “Reconfigurable intelligent surface aided NOMA networks,” *IEEE Journal on Selected Areas in Communications*, vol. 38, no. 11, pp. 2575–2588, 2020.
- [28] Zhou, Shaoqing and Xu, Wei and Wang, Kezhi and Di Renzo, Marco and Alouini, Mohamed-Slim, “Spectral and energy efficiency of irs-assisted

miso communication with hardware impairments," *IEEE Wireless Communications Letters*, vol. 9, no. 9, pp. 1366–1369, 2020.

[29] X. GUAN and Q. WU, "IRS-Enabled Spectrum Sharing: Interference Modeling, Channel Estimation and Robust Passive Beamforming," *ZTE Communications*, vol. 20, no. 1, pp. 28–35, 2022.

[30] Z. Ji, Z. Qin, and C. G. Parini, "Reconfigurable intelligent surface aided cellular networks with device-to-device users," *IEEE Transactions on Communications*, vol. 70, no. 3, pp. 1808–1819, 2022.

[31] C. Liaskos, L. Mamatas, A. Pourdamghani, A. Tsoliariadi, S. Ioannidis, A. Pitsillides, S. Schmid, and I. F. Akyildiz, "Software-defined reconfigurable intelligent surfaces: From theory to end-to-end implementation," *Proceedings of the IEEE*, vol. 110, no. 9, pp. 1466–1493, 2022.

[32] A. Banchs, M. Fiore, A. Garcia-Saavedra, and M. Gramaglia, "Network intelligence in 6G: Challenges and opportunities," in *Proceedings of the 16th ACM Workshop on Mobility in the Evolving Internet Architecture*, 2021, pp. 7–12.

[33] S. Basharat, M. Khan, M. Iqbal, U. S. Hashmi, S. A. R. Zaidi, and I. Robertson, "Exploring reconfigurable intelligent surfaces for 6G: State-of-the-art and the road ahead," *IET Communications*, vol. 16, no. 13, pp. 1458–1474, 2022.

[34] Y. Liu, X. Liu, X. Mu, T. Hou, J. Xu, M. Di Renzo, and N. Al-Dahir, "Reconfigurable intelligent surfaces: Principles and opportunities," *IEEE Communications Surveys & Tutorials*, vol. 23, no. 3, pp. 1546–1577, 2021.

[35] X. Mu, Y. Liu, L. Guo, J. Lin, and N. Al-Dahir, "Capacity and optimal resource allocation for IRS-assisted multi-user communication systems," *IEEE Transactions on Communications*, vol. 69, no. 6, pp. 3771–3786, 2021.

[36] A. Elzanaty, A. Guerra, F. Guidi, and M.-S. Alouini, "Reconfigurable intelligent surfaces for localization: Position and orientation error bounds," *IEEE Transactions on Signal Processing*, vol. 69, pp. 5386–5402, 2021.

[37] H. Yang, Z. Xiong, J. Zhao, D. Niyato, Q. Wu, H. V. Poor, and M. Tornatore, "Intelligent reflecting surface assisted anti-jamming communications: A fast reinforcement learning approach," *IEEE Transactions on Wireless Communications*, vol. 20, no. 3, pp. 1963–1974, 2020.

[38] N. M. Salih, M. Aldababsa, and K. Yahya, "Enhancing UAV communication links with Reconfigurable intelligent surfaces," *AEU-International Journal of Electronics and Communications*, vol. 171, p. 154933, 2023.

[39] M. Diamanti, M. Tsampazi, E. E. Tsiropoulou, and S. Papavassiliou, "Energy efficient multi-user communications aided by reconfigurable intelligent surfaces and UAVs," in *IEEE International Conference on Smart Computing (SMARTCOMP)*, 2021, pp. 371–376.

[40] S. Li, B. Duo, X. Yuan, Y.-C. Liang, and M. Di Renzo, "Reconfigurable intelligent surface assisted UAV communication: Joint trajectory design and passive beamforming," *Wireless Communications Letters*, vol. 9, no. 5, pp. 716–720, 2020.

[41] S. Basharat, S. A. Hassan, H. Pervaiz, A. Mahmood, Z. Ding, and M. Gidlund, "Reconfigurable intelligent surfaces: Potentials, applications, and challenges for 6G wireless networks," *Wireless Communications*, vol. 28, no. 6, pp. 184–191, 2021.

[42] Z. Ning, T. Li, Y. Wu, X. Wang, Q. Wu, F. R. Yu, and S. Guo, "Intelligent-Reflecting-Surface-Assisted UAV Communications for 6G Networks," *arXiv preprint arXiv:2310.20242*, 2023.

[43] Y. Yu, X. Liu, and V. C. Leung, "Fair downlink communications for RIS-UAV enabled mobile vehicles," *Wireless Communications Letters*, vol. 11, no. 5, pp. 1042–1046, 2022.

[44] MATLAB R2021a, The Mathworks, Inc., Natick, Massachusetts, 2021.

[45] QuaDRiGa Source Code GitHub repository. <https://github.com/fraunhoferhhi/QuaDRiGa>.

[46] L. Bonati, P. Johari, M. Polese, S. D’Oro, S. Mohanti, M. Tehrani-Moayyed, D. Villa, S. Shrivastava, C. Tassie, K. Yoder, A. Bagga, P. Patel, V. Petkov, M. Seltser, F. Restuccia, A. Gosain, K. R. Chowdhury, S. Basagni, and T. Melodia, "Colosseum: Large-Scale Wireless Experimentation Through Hardware-in-the-Loop Network Emulation," in *Proc. of IEEE Intl. Symp. on Dynamic Spectrum Access Networks (DySPAN)*, Virtual Conference, December 2021.

[47] E. Basar and I. Yildirim, "Reconfigurable intelligent surfaces for future wireless networks: A channel modeling perspective," *IEEE Wireless Communications*, vol. 28, no. 3, pp. 108–114, 2021.

[48] E. Basar, and I. Yildirim, "SimRIS channel simulator for reconfigurable intelligent surface-empowered communication systems," in *Latin-American Conference on Communications (LATINCOM)*. IEEE, 2020, pp. 1–6.

[49] B. Sihlbom, M. I. Poulakis, and M. Di Renzo, "Reconfigurable intelligent surfaces: Performance assessment through a system-level simulator," *Wireless Communications*, 2022.

[50] Y. Sun, C.-X. Wang, J. Huang, and J. Wang, "A 3D non-stationary channel model for 6G wireless systems employing intelligent reflecting surfaces with practical phase shifts," *IEEE Transactions on Cognitive Communications and Networking*, vol. 7, no. 2, pp. 496–510, 2021.

[51] J. Dang, S. Gao, Y. Zhu, R. Guo, H. Jiang, Z. Zhang, L. Wu, B. Zhu, and L. Wang, "A geometry-based stochastic channel model and its application for intelligent reflecting surface assisted wireless communication," *IET Communications*, vol. 15, no. 3, pp. 421–434, 2021.

[52] M. Dajer, Z. Ma, L. Piazzoli, N. Prasad, X.-F. Qi, B. Sheen, J. Yang, and G. Yue, "Reconfigurable intelligent surface: Design the channel—A new opportunity for future wireless networks," *Digital Communications and Networks*, vol. 8, no. 2, pp. 87–104, 2022.

[53] H. Zhou, M. Erol-Kantarci, Y. Liu, and H. V. Poor, "A survey on model-based, heuristic, and machine learning optimization approaches in ris-aided wireless networks," *IEEE Communications Surveys & Tutorials*, 2023.

[54] L. Kong, J. He, Y. Ai, S. Chatzinotas, and B. Ottersten, "Channel modeling and analysis of reconfigurable intelligent surfaces assisted vehicular networks," in *International Conference on Communications Workshops (ICC Workshops)*. IEEE, 2021, pp. 1–6.

[55] Z. Tian, Z. Chen, M. Wang, Y. Jia, and W. Wen, "Reconfigurable intelligent surface-aided spectrum sharing coexisting with multiple primary networks," in *IEEE Wireless Communications and Networking Conference (WCNC)*, 2023, pp. 1–6.

[56] Y. Chen, Y. Wang, J. Zhang, and M. Di Renzo, "QoS-driven spectrum sharing for reconfigurable intelligent surfaces (RISs) aided vehicular networks," *IEEE Transactions on Wireless Communications*, vol. 20, no. 9, pp. 5969–5985, 2021.

[57] A.-A. A. Boulogeorgos and A. Alexiou, "Coverage analysis of reconfigurable intelligent surface assisted THz wireless systems," *IEEE Open Journal of Vehicular Technology*, vol. 2, pp. 94–110, 2021.

[58] E. Björnson, H. Wymeersch, B. Matthesen, P. Popovski, L. Sanguinetti, and E. de Carvalho, "Reconfigurable intelligent surfaces: A signal processing perspective with wireless applications," *IEEE Signal Processing Magazine*, vol. 39, no. 2, pp. 135–158, 2022.

[59] X. Yu, V. Jamali, D. Xu, D. W. K. Ng, and R. Schober, "Smart and reconfigurable wireless communications: From irs modeling to algorithm design," *Wireless Communications*, vol. 28, no. 6, pp. 118–125, 2021.

[60] J. Xu, X. Mu, and Y. Liu, "Exploiting STAR-RISs in near-field communications," *IEEE Transactions on Wireless Communications*, 2023.

[61] W. Tang, X. Chen, M. Z. Chen, J. Y. Dai, Y. Han, S. Jin, Q. Cheng, G. Y. Li, and T. J. Cui, "On channel reciprocity in reconfigurable intelligent surface assisted wireless networks," *Wireless Communications*, vol. 28, no. 6, pp. 94–101, 2021.

[62] L. G. da Silva, Z. Chu, P. Xiao, and A. Cerqueira S Jr, "A varactor-based 1024-element RIS design for mm-waves," *Frontiers in Communications and Networks*, vol. 4, p. 1086011, 2023.

[63] Y. Liu, J. Dou, Y. Cui, Y. Chen, J. Yang, F. Qin, and Y. Wang, "Reconfigurable Intelligent Surface Physical Model in Channel Modeling," *Electronics*, vol. 11, no. 17, p. 2798, 2022.

[64] R. Liu, J. Dou, P. Li, J. Wu, and Y. Cui, "Simulation and field trial results of reconfigurable intelligent surfaces in 5g networks," *IEEE Access*, vol. 10, pp. 122 786–122 795, 2022.

[65] M. Rossanese, P. Mursia, A. Garcia-Saavedra, V. Sciancalepore, A. Asadi, and X. Costa-Perez, "Designing, building, and characterizing RF switch-based reconfigurable intelligent surfaces," in *Proceedings of the 16th ACM Workshop on Wireless Network Testbeds, Experimental evaluation & Characterization*, 2022, pp. 69–76.

[66] C. Huang, A. Zappone, G. C. Alexandropoulos, M. Debbah, and C. Yuen, "Reconfigurable Intelligent Surfaces for Energy Efficiency in Wireless Communication," *IEEE Transactions on Wireless Communications*, vol. 18, no. 8, pp. 4157–4170, 2019.

[67] X. Yu, G. Wang, X. Huang, K. Wang, W. Xu, and Y. Rui, "Energy Efficient Resource Allocation for Uplink RIS-Aided Millimeter-Wave Networks With NOMA," *IEEE Transactions on Mobile Computing*, vol. 23, no. 1, pp. 423–436, 2024.

[68] A. A. Deshpande, C. J. Vacca-Rubio, S. Mohebi, D. Salami, E. de Carvalho, P. Popovski, S. Sigg, M. Zorzi, and A. Zanella, "Energy-efficient design for ris-assisted uav communications in beyond-5g networks," in *2022 20th Mediterranean Communication and Computer Networking Conference (MedComNet)*, 2022, pp. 158–165.

[69] M. Ahsan, S. Jamil, M. T. Ejaz, and M. S. Abbas, "Energy efficiency maximization in ris-assisted wireless networks," in *2021 International Conference on Computing, Electronic and Electrical Engineering (ICE Cube)*, 2021, pp. 1–6.

[70] R. K. Fotock, A. Zappone, and M. D. Renzo, "Energy Efficiency Maximization in RIS-aided Networks with Global Reflection Constraints,"

in *ICASSP 2023 - 2023 IEEE International Conference on Acoustics, Speech and Signal Processing (ICASSP)*, 2023, pp. 1–5.

[71] Y. Zhang, Y. Lu, R. Zhang, B. Ai, and D. Niyato, “Deep reinforcement learning for secrecy energy efficiency maximization in ris-assisted networks,” *IEEE Transactions on Vehicular Technology*, vol. 72, no. 9, pp. 12 413–12 418, 2023.

[72] Y. Guo, F. Fang, D. Cai, and Z. Ding, “Energy-Efficient Design for a NOMA Assisted STAR-RIS Network With Deep Reinforcement Learning,” *IEEE Transactions on Vehicular Technology*, vol. 72, no. 4, pp. 5424–5428, 2023.

[73] M. Diamanti, P. Charatsaris, E. E. Tsiropoulou, and S. Papavassiliou, “The prospect of reconfigurable intelligent surfaces in integrated access and backhaul networks,” *IEEE Transactions on Green Communications and Networking*, vol. 6, no. 2, pp. 859–872, 2021.

[74] M. Tehrani-Moayyed, L. Bonati, P. Johari, T. Melodia, and S. Basagni, “Creating RF Scenarios for Large-Scale, Real-Time Wireless Channel Emulators,” in *Proceedings of IEEE MedComNet*, 2021.

[75] D. Villa, M. Tehrani-Moayyed, P. Johari, S. Basagni, and T. Melodia, “CaST: a toolchain for creating and characterizing realistic wireless network emulation scenarios,” in *Proceedings of the 16th ACM Workshop on Wireless Network Testbeds, Experimental evaluation & CCharacterization*, 2022, pp. 45–52.

[76] R. Rusca, F. Raviglione, C. Casetti, P. Giaccone, and F. Restuccia, “Mobile RF Scenario Design for Massive-Scale Wireless Channel Emulators,” in *Joint European Conference on Networks and Communications & 6G Summit (EuCNC/6G Summit)*. IEEE, 2023, pp. 675–680.

[77] S. Lasaulce, Y. Hayel, R. El Azouzi, and M. Debbah, “Introducing hierarchy in energy games,” *IEEE Transactions on Wireless Communications*, vol. 8, no. 7, pp. 3833–3843, 2009.

[78] G. He, S. Lasaulce, and Y. Hayel, “Stackelberg games for energy-efficient power control in wireless networks,” in *2011 Proceedings IEEE INFOCOM*. IEEE, 2011, pp. 591–595.

[79] srsRAN website. <https://www.srslte.com/>. Accessed September 2022.

[80] “Google Maps,” [Online]. Available: <https://www.google.com/maps>.

[81] S. Ju, O. Kanhere, Y. Xing, and T. S. Rappaport, “A millimeter-wave channel simulator NYUSIM with spatial consistency and human blockage,” in *IEEE global communications conference (GLOBECOM)*, 2019, pp. 1–6.

[82] P. Kyosti, J. Meinila, L. Hentila, X. Zhao, T. Jamsa, C. Schneider, M. Narandzic, M. Milojevic, A. Hong, J. Ylitalo *et al.*, “IST-4-027756 WINNER II D1. 1.2 V1. 2: WINNER II channel models,” Available: www.ist-winner.org, 2007.

[83] F. Ademaj, M. Taranetz, and M. Rupp, “3GPP 3D MIMO channel model: A holistic implementation guideline for open source simulation tools,” *EURASIP Journal on Wireless Communications and Networking*, no. 1, pp. 1–14, 2016.

[84] L. Pang, J. Zhang, Y. Zhang, X. Huang, Y. Chen, and J. LI, “Investigation and Comparison of 5G Channel Models: From QuaDRiGa, NYUSIM, and MG5G Perspectives,” *Chinese Journal of Electronics*, vol. 31, no. 1, pp. 1–17, 2022.

[85] B. Mondal, T. A. Thomas, E. Visotsky, F. W. Vook, A. Ghosh, Y.-H. Nam, Y. Li, J. Zhang, M. Zhang, Q. Luo *et al.*, “3D channel model in 3GPP,” *IEEE Communications Magazine*, vol. 53, no. 3, pp. 16–23, 2015.

[86] S. Jaeckel, L. Raschkowski, K. Boerner, and L. Thiele, “F. Burkhardt, E. Eberlein, “QuaDRiGa-Quasi Deterministic Radio Channel Generator,” User Manual and Documentation,” Tech. Rep. v2. 2.0, Fraunhofer Heinrich Hertz Institute, Tech. Rep., 2019, [Online]. Available: https://github.com/fraunhoferhhi/QuaDRiGa/blob/main/quadriga-documentation_v2.6.1-0.pdf.

[87] S. Jaeckel, L. Raschkowski, K. Börner, and L. Thiele, “QuaDRiGa: A 3-D multi-cell channel model with time evolution for enabling virtual field trials,” *IEEE transactions on antennas and propagation*, vol. 62, no. 6, pp. 3242–3256, 2014.

[88] M. E. Ranjesh and A. A. Khazaei, “The Optimized QuaDRiGa WiFi Channel Model,” *International Journal of Science and Engineering Investigations*, vol. 4, no. 9, pp. 51–61, 2015.

[89] “Intelligent Transport Systems (ITS); Access Layer; Part 1: Channel Models for the 5,9 GHz frequency band”. Sophia Antipolis Cedex, FRANCE, ETSI TR 103 257-1 V1.1.1, Tech. Rep., May, 2019. [Online]. Available: https://www.etsi.org/deliver/etsi_tr/103200_103299/10325701/01.01.01_60/tr_10325701v010101p.pdf.

[90] Y. He, Y. Zhang, J. Zhang, L. Pang, Y. Chen, and G. Ren, “Investigation and Comparison of QuaDRiGa, NYUSIM and MG5G Channel Models for 5G Wireless Communications,” in *IEEE 92nd Vehicular Technology Conference (VTC2020-Fall)*, 2020, pp. 1–5.

[91] ETSI TR 138 901 V14.3.0 (2018-01). [Online]. Available: https://www.etsi.org/deliver/etsi_tr/138900_138999/138901/14.03.00_60/tr_138901v140300p.pdf.

[92] C. Arunachalaperumal, S. Dhilipkumar, and G. Abija, “Enhanced 3D MIMO channel for urban macro environment,” *International Journal of Pure and Applied Mathematics, Special Issue*, vol. 118, no. 10, pp. 259–269, 2018.

[93] M. Giordani, T. Shimizu, A. Zanella, T. Higuchi, O. Altintas, and M. Zorzi, “Path loss models for V2V mmWave communication: performance evaluation and open challenges,” in *IEEE Connected and Automated Vehicles Symposium (CAVS)*. IEEE, 2019, pp. 1–5.

[94] C. F. Mecklenbrauker, A. F. Molisch, J. Karedal, F. Tufvesson, A. Paier, L. Bernadó, T. Zemen, O. Klemp, and N. Czink, “Vehicular channel characterization and its implications for wireless system design and performance,” *Proceedings of the IEEE*, vol. 99, no. 7, pp. 1189–1212, 2011.

[95] U.S. Naval Research Laboratory, “Multi-Generator (MGEN) Network Test Tool”. <https://www.nrl.navy.mil/itd/ncs/products/mgen>. 2019.

[96] B. Bloessl, M. Segata, C. Sommer, and F. Dressler, “Performance assessment of IEEE 802.11 p with an open source SDR-based prototype,” *IEEE transactions on mobile computing*, vol. 17, no. 5, pp. 1162–1175, 2017.

[97] A. A. Khan, A. A. Laghari, M. Shafiq, S. A. Awan, and Z. Gu, “Vehicle to everything (V2X) and edge computing: A secure lifecycle for UAV-assisted vehicle network and offloading with blockchain,” *Drones*, vol. 6, no. 12, p. 377, 2022.

[98] ETSI, “Reconfigurable Intelligent Surfaces (RIS); Use Cases, Deployment Scenarios and Requirements,” ETSI, ETSI Group Report RIS 001 V1.1.1, April 2023. [Online]. Available: https://www.etsi.org/deliver/etsi_gr/RIS/001_0099/001/01.01_60/gr_RIS001v010101p.pdf

[99] L. C. Paul, H. K. Saha, T. Rani, M. Z. Mahmud, T. K. Roy, W.-S. Lee *et al.*, “An Omni-Directional Wideband Patch Antenna with Parasitic Elements for Sub-6 GHz Band Applications,” *International Journal of Antennas and Propagation*, 2022.

[100] R. Azim, A. M. H. Meaze, A. Affandi, M. M. Alam, R. Aktar, M. S. Mia, T. Alam, M. Samsuzzaman, and M. T. Islam, “A multi-slotted antenna for LTE/5G Sub-6 GHz wireless communication applications,” *International Journal of Microwave and Wireless Technologies*, vol. 13, no. 5, pp. 486–496, 2021.

[101] T. Rani, S. C. Das, M. S. Hossen, L. C. Paul, and T. K. Roy, “Development of a Broadband Antenna for 5G Sub-6 GHz Cellular and IIoT Smart Automation Applications,” in *12th International Conference on Electrical and Computer Engineering (ICECE)*. IEEE, 2022, pp. 465–468.

[102] M. S. Sharawi, M. Ikram, and A. Shamim, “A two concentric slot loop based connected array MIMO antenna system for 4G/5G terminals,” *IEEE Transactions on antennas and propagation*, vol. 65, no. 12, pp. 6679–6686, 2017.

[103] B. De Beelde, E. Tanghe, M. Yusuf, D. Plets, and W. Joseph, “Radio channel modeling in a ship hull: Path loss at 868 MHz and 2.4, 5.25, and 60 GHz,” *IEEE Antennas and Wireless Propagation Letters*, vol. 20, no. 4, pp. 597–601, 2021.

[104] A. Zaidi, W. A. Awan, N. Hussain, and A. Baghdad, “A Wide and Tri-band Flexible Antennas with Independently Controllable Notch Bands for Sub-6-GHz Communication System,” *Radioengineering*, vol. 29, no. 1, 2020.

[105] C.-X. Mao, M. Khalily, P. Xiao, T. W. Brown, and S. Gao, “Planar sub-millimeter-wave array antenna with enhanced gain and reduced side-lobes for 5G broadcast applications,” *IEEE Transactions on Antennas and Propagation*, vol. 67, no. 1, pp. 160–168, 2018.

[106] S. Ranvier, S. Dudorov, M. Kyro, C. Luxey, C. Icheln, R. Staraj, and P. Vainikainen, “Low-cost planar omnidirectional antenna for mm-wave applications,” *IEEE Antennas and Wireless Propagation Letters*, vol. 7, pp. 521–523, 2008.

[107] K. Fan, Z.-C. Hao, Q. Yuan, J. Hu, G. Q. Luo, and W. Hong, “Wideband horizontally polarized omnidirectional antenna with a conical beam for millimeter-wave applications,” *IEEE Transactions on Antennas and Propagation*, vol. 66, no. 9, pp. 4437–4448, 2018.

[108] G. R. MacCartney, T. S. Rappaport, M. K. Samimi, and S. Sun, “Millimeter-wave omnidirectional path loss data for small cell 5G channel modeling,” *IEEE access*, vol. 3, pp. 1573–1580, 2015.

[109] M. N. Hasan, S. Bashir, and S. Chu, “Dual band omnidirectional millimeter wave antenna for 5G communications,” *Journal of Electromagnetic Waves and Applications*, vol. 33, no. 12, pp. 1581–1590, 2019.

[110] S. Sun, G. R. MacCartney, M. K. Samimi, and T. S. Rappaport, “Synthesizing omnidirectional antenna patterns, received power and path loss from directional antennas for 5G millimeter-wave communications,”

in *IEEE Global Communications Conference (GLOBECOM)*. IEEE, 2015, pp. 1–7.

[111] M. Abirami, “A review of patch antenna design for 5G,” in *IEEE International Conference on Electrical, Instrumentation and Communication Engineering (ICEICE)*. IEEE, 2017, pp. 1–3.

[112] Y. Niu, Y. Li, D. Jin, L. Su, and A. V. Vasilakos, “A survey of millimeter wave communications (mmWave) for 5G: opportunities and challenges,” *Wireless networks*, vol. 21, pp. 2657–2676, 2015.

[113] H. K. Pan, “Dual-polarized Mm-wave phased array antenna for multi-Gb/s 60GHz communication,” in *IEEE International Symposium on Antennas and Propagation (APSURSI)*. IEEE, 2011, pp. 3279–3282.

[114] C. X. Mao, M. Khalily, L. Zhang, P. Xiao, Y. Sun, and D. H. Werner, “Compact patch antenna with vertical polarization and omnidirectional radiation characteristics,” *IEEE Transactions on Antennas and Propagation*, vol. 69, no. 2, pp. 1158–1161, 2020.

[115] E. E. Tsiroupolou, P. Vamvakas, G. K. Katsinis, and S. Papavassiliou, “Combined power and rate allocation in self-optimized multi-service two-tier femtocell networks,” *Computer Communications*, vol. 72, pp. 38–48, 2015.

[116] ETSI, “5G; NR; User Equipment (UE) radio transmission and reception; Part 1: Range 1 Standalone (3GPP TS 38.101-1 version 17.5.0 Release 17),” https://www.etsi.org/deliver/etsi_ts/138100_138199/13810101/17.05.00_60/ts_13810101v170500p.pdf, May 2022, ETSI TS 138 101-1 V17.5.0 (2022-05).

[117] ETSI, “5G; NR; User Equipment (UE) radio transmission and reception; Part 2: Range 2 Standalone (3GPP TS 38.101-2 version 17.5.0 Release 17),” ETSI, Tech. Rep. ETSI TS 138 101-2 V17.5.0, April 2022, available online. [Online]. Available: https://www.etsi.org/deliver/etsi_ts/138100_138199/13810102/17.05.00_60/ts_13810102v170500p.pdf

[118] ETSI, “LTE; Evolved Universal Terrestrial Radio Access (E-UTRA); Physical layer procedures (3GPP TS 36.213 version 14.2.0 Release 14),” https://www.etsi.org/deliver/etsi_ts/136200_136299/136213/14.02.00_60/ts_136213v140200p.pdf, April 2017, ETSI TS 136 213 V14.2.0 (2017-04).

[119] V. Tapió, I. Hemadeh, A. Mourad, A. Shoaieifard, and M. Juntti, “Survey on reconfigurable intelligent surfaces below 10 GHz,” *EURASIP Journal on Wireless Communications and Networking*, pp. 1–18, 2021.

[120] E. Björnson, Ö. Özdogan, and E. G. Larsson, “Reconfigurable intelligent surfaces: Three myths and two critical questions,” *IEEE Communications Magazine*, vol. 58, no. 12, pp. 90–96, 2020.

[121] M. Z. Siddiqi and T. Mir, “Reconfigurable intelligent surface-aided wireless communications: An overview,” *Intelligent and Converged Networks*, vol. 3, no. 1, pp. 33–63, 2022.

[122] D. Villa, D. Uvaydov, L. Bonati, P. Johari, J. M. Jornet, and T. Melodia, “Twining Commercial Radio Waveforms in the Colosseum Wireless Network Emulator,” in *Proceedings of the 17th ACM Workshop on Wireless Network Testbeds, Experimental evaluation & Characterization*, 2023, pp. 33–40.

[123] L. Bonati, S. D’Oro, S. Basagni, and T. Melodia, “SCOPE: An open and softwareized prototyping platform for NextG systems,” in *Proceedings of the 19th Annual International Conference on Mobile Systems, Applications, and Services*, 2021, pp. 415–426.

[124] I. Gomez-Miguelez, A. Garcia-Saavedra, P. D. Sutton, P. Serrano, C. Cano, and D. J. Leith, “srsLTE: An Open-Source Platform for LTE Evolution and Experimentation,” in *Proceedings of the Tenth ACM International Workshop on Wireless Network Testbeds, Experimental Evaluation, and Characterization*, 2016, pp. 25–32.

[125] M. Tsampazi, S. D’Oro, M. Polese, L. Bonati, G. Poitau, M. Healy, and T. Melodia, “A Comparative Analysis of Deep Reinforcement Learning-based xApps in O-RAN,” *IEEE Global Communications Conference (GLOBECOM)*, 2023.

[126] M. Tsampazi, S. D’Oro, M. Polese, L. Bonati, G. Poitau, M. Healy, M. Alavirad, and T. Melodia, “PandORA: Automated Design and Comprehensive Evaluation of Deep Reinforcement Learning Agents for Open RAN,” *arXiv preprint arXiv:2407.11747*, 2024.



Maria Tsampazi received her MEng Degree in Electrical and Computer Engineering from National Technical University of Athens, Greece in 2021. She is a Ph.D. Candidate in Electrical Engineering at the Institute for the Wireless Internet of Things at Northeastern University, Boston, MA, USA. Her research interests focus on NextG wireless networks and intelligent resource allocation in Open RAN. She has received academic awards sponsored by the U.S. National Science Foundation, the IEEE Communications Society, and Northeastern University, and is a 2024 recipient of the National Spectrum Consortium Women in Spectrum Scholarship. She has previously collaborated with both government and industry, including organizations such as the U.S. Department of Transportation and Dell Technologies.



Tommaso Melodia is the William Lincoln Smith Chair Professor with the Department of Electrical and Computer Engineering at Northeastern University in Boston. He is also the Founding Director of the Institute for the Wireless Internet of Things and the Director of Research for the PAWR Project Office. He received his Ph.D. in Electrical and Computer Engineering from the Georgia Institute of Technology in 2007. He is a recipient of the National Science Foundation CAREER award. Prof. Melodia has served as Associate Editor of IEEE Transactions on Wireless Communications, IEEE Transactions on Mobile Computing, Elsevier Computer Networks, among others. He has served as Technical Program Committee Chair for IEEE INFOCOM 2018, General Chair for IEEE SECON 2019, ACM Nanocom 2019, and ACM WUWnet 2014. Prof. Melodia is the Director of Research for the Platforms for Advanced Wireless Research (PAWR) Project Office, a 100M public-private partnership to establish 4 city-scale platforms for wireless research to advance the US wireless ecosystem in years to come. Prof. Melodia’s research on modeling, optimization, and experimental evaluation of Internet-of-Things and wireless networked systems has been funded by the National Science Foundation, the Air Force Research Laboratory the Office of Naval Research, DARPA, and the Army Research Laboratory. Prof. Melodia is a Fellow of the IEEE and a Senior Member of the ACM.